Master's thesis

NTNU
Norwegian University of Science and Technology
Faculty of Information Technology and Electrical Engineering
Department of Engineering Cybernetics

Daniel Dreyer Svendsen

Implementation and Comparison of Nonlinear State of Charge Estimators using Equivalent Circuit Models for Two Lithium-Ion Battery Cell Chemistries

Master's thesis in Cybernetics and Robotics
Supervisor: Damiano Varagnolo
Co-supervisor: Walter Caharija and Daniel Grübl
June 2023

NTNU
Norwegian University of
Science and Technology

Daniel Dreyer Svendsen

Implementation and Comparison of Nonlinear State of Charge Estimators using Equivalent Circuit Models for Two Lithium-Ion Battery Cell Chemistries

Master's thesis in Cybernetics and Robotics
Supervisor: Damiano Varagnolo
Co-supervisor: Walter Caharija and Daniel Grübl
June 2023

Norwegian University of Science and Technology
Faculty of Information Technology and Electrical Engineering
Department of Engineering Cybernetics

NTNU
Norwegian University of
Science and Technology

Abstract

Lithium-ion batteries are extensively used as an energy storage technology. They provide benefits such as low weight, high energy density, and durability, and can be pivotal in the process of reaching climate neutrality. Continuous optimization of the batteries' operation and safety is essential, where monitoring important internal states such as the State of Charge is a fundamental part. This state cannot be directly measured and must be estimated by a battery management system purely based on current and voltage measurements. For model-based estimation, accurate lithium-ion battery models are necessary. These models are not easy to produce due to the batteries' nonlinear behavior and sensitivity to noise.

This thesis implements and compares three nonlinear State of Charge (SOC) estimators with three different equivalent circuit models for two different lithium-ion battery cells. The estimators are the Extended Kalman filter (EKF), the Sigma Point Kalman filter (SPKF), and the Moving Horizon Estimator (MHE). The models are the Rint (R) model, the Thevenin (1RC) model, and the enhanced self-correcting (ESC) model, presented in order of increasing complexity. All combinations of the estimators and models are implemented and evaluated using battery data for an NMC cell and an LFP cell, which both represent two commonly used cell chemistries in lithium-ion batteries. Here dynamic load current profiles retrieved from an Electric Vehicle (EV) are used as input for performance evaluation. The cell types demonstrate different characteristics, of which their open-circuit voltage is of great importance for SOC estimation.

The results showed that the estimators demonstrated a very similar SOC estimation performance in three different simulation scenarios. This was true for many of the model-cell combinations, where it can be argued that the 1RC model offered the overall best performance. The estimation accuracy was considerably worse for the LFP cell when compared to the NMC cell. This was likely due to the flat open-circuit voltage characteristics of the LFP cell inflicting observability issues on the models. The SOC root-mean-square estimation error reached as low as approximately 0.45 % for the NMC cell using the 1RC or ESC model, and as low as 2.74 % for the LFP cell using the R model. The latter result was inconsistent with what kind of EV load current profile was applied to the LFP models. Due to the heavy computational complexity of the MHE, and the theoretical complexity of the SPKF, it was concluded that the EKF marginally was the better-performing estimator.

Sammendrag

Litium-ion-batterier blir omfattende brukt som en energilagringsløsning. De gir fordeler som lav vekt, høy energitetthet og holdbarhet, og kan være avgjørende for å oppnå klimanøytralitet. Kontinuerlig optimalisering av batterienes drift og sikkerhet er viktig, der overvåking av viktige interne tilstander som restkapasitet er en grunnleggende del. Denne tilstanden kan ikke måles direkte og må derfor estimeres av et batteristyringssystem basert utelukkende på strøm- og spenningsmålinger. Nøyaktige litium-ion-batterimodeller er nødvendige for modellbasert estimering. Disse modellene er ikke enkle å produsere på grunn av batterienes ulineære oppførsel og sensitivitet for støy.

Denne masteroppgaven implementerer og sammenligner tre ulineære tilstandsestimatorer for restkapasiteten med tre forskjellige ekvivalent-krets modeller for to ulike litium-ion-battericeller. Estimatorene er det utvidede Kalman-filteret (EKF), et sigma-punkts Kalman-filteret (SPKF) og en bevegelig horisont estimator (MHE). Modellene er Rint (R) modellen, Thevenin (1RC) modellen og den forbedrede selvjusterende (ESC) modellen, presentert i stigende kompleksitet. Alle kombinasjonene av estimatorer og modeller ble implementert og evaluert ved bruk av batteridata for en NMC-celle og en LFP-celle, som begge representerer to vanlig brukte cellekjemier i litium-ion-batterier. Her brukes dynamiske belastningsstrømprofiler hentet fra en elektrisk bil som inngangssignal for prestasjonsvurdering. Celletypene viser forskjellige egenskaper, hvor åpenkretsspenningen deres er av stor betydning for estimering av restkapasiteten.

Resultatene viste at estimatorene hadde svært lik ytelse for restkapasitetsestimering i tre forskjellige simuleringscenarier. Dette gjaldt for mange av kombinasjonene av modell og celle, der det kan hevdes at 1RC-modellen ga den beste totale ytelsen. Videre var det tydelig at estimatnøyaktigheten var betydelig dårligere for LFP-cellen sammenlignet med NMC-cellen. Dette skyldtes antakeligvis den flate karakteristikken til åpenkretsspenningen for LFP-cellen, som reduserte modellenes observerbarhet. Den kvadratisk gjennomsnittlige feilen i estimert restkapasitet nådde så lavt som omtrent 0,45 % for NMC-cellen ved bruk av 1RC- eller ESC- modellen, og så lavt som 2,74 % for LFP-cellen ved bruk av R-modellen. Det siste resultatet var inkonsistent med hvilken type belastningsstrømprofil som ble brukt for LFP-modellene. På grunn av den tunge beregningskompleksiteten til MHE og den teoretiske kompleksiteten til SPKF, ble det konkludert med at EKF marginalt var den bedre ytende estimatoren.

Preface

This master's thesis is a culmination of five years at the M.Sc. Cybernetics and Robotics study programme at NTNU in Trondheim. The work herein is a continuation of the specialization project conducted during the fall semester of 2022, which also focused on State of Charge estimation and was written by the same author. There the emphasis was put on laying a foundation for the master's thesis by focusing on linear estimation methods as well as preliminary nonlinear state estimation. Here it should be mentioned that some of the sections in this master's thesis have been carried over from the specialization project with minor modifications. These include parts of the introduction, the section on the theory of lithium-ion batteries, the chapter on the modeling of batteries, and to some extent the chapter presenting the nonlinear state estimators. Both theses have been completed in collaboration and consultation with Siemens Energy, which turned out to be particularly motivating and educational. The material in this thesis is mainly meant for a reader with a background in cybernetics, battery technology, or similar, where state estimation is a central part.

I would like to extend my gratitude to my supervisor, Damiano Varagnolo, for letting me complete this thesis with freedom and providing me with insightful guidance along the way. I am equally grateful to my co-supervisors, Walter Caharija and Daniel Grübl from Siemens Energy, for their close follow-up on a weekly basis and encouragement and support throughout both semesters, ensuring that progress was made.

Finally, I am grateful to my family for their continuing support.

Daniel Dreyer Svendsen

Trondheim, June 2023

Table of Contents

List of Tables

List of Figures

Abbreviations

Abbreviation	Description
BMS	Battery Management System
BOL	Beginning Of Life
CALCE	Center for Advanced Life Cycle Engineering
CDKF	Central Difference Kalman Filter
DST	Dynamic Stress Test
ECM	Equivalent-Circuit Model
EIS	Electrochemical Impedance Spectrum
EKF	Extended Kalman Filter
END	End Of Life
ESC	Enhanced Self-Correcting
EV	Electric Vehicle
FUDS	Federal Urban Driving Schedule
GHG	Greenhouse Gas
ICEV	Internal Combustion Engine Vehicle
IMO	International Maritime Organization
LIB	Lithium-Ion Battery
LFP	Lithium Iron Phosphate
MAE	Mean Absolute Error
MAP	Maximum A Posteriori
MHE	Moving Horizon Estimator
NLP	Nonlinear Programming
NMC	Nickel Manganese Cobalt Oxide
OCV	Open-Circuit Voltage
OCP	Optimal Control Problem
RC	Resistor-Capacitor
RMSE	Root Mean Square Error
RMS	Root Mean Square
SOC	State of Charge
SOE	State of Energy
SOH	State of Health
SOP	State of Power
SPKF	Sigma-Point Kalman Filter
UKF	Unscented Kalman Filter
US06	United States Highway 06
USABC	United States Advanced Battery Consortium

1

Introduction

1.1 Background

The usage of Lithium-Ion Batteries (LIBs) as an energy storage technology is widespread and continues to grow across various applications. LIBs offer significant advantages such as high energy density, lightweight design, and long lifespan, and can be instrumental in achieving energy sustainability [1]. Particularly in Electric Vehicles (EVs) like electric cars and electric ships, where safety and reliability are essential [2], LIBs have emerged as a preferred power source. It is expected that the cost of batteries will decline to 150 €/kWh by 2025, which implies that an EV can reach cost parity with the Internal-Combustion-Engine Vehicle (ICEV) in a few years' time, making it economically viable to continue developing EVs [3]. In worldwide transport, the total number of EVs on roads is predicted to exceed 300 million by 2030, where the required installed capacity of LIBs will be around 3000 GWh [4]. In the maritime sector, there is an ambition to decrease Greenhouse Gas (GHG) emissions by at least 40 % by 2030 and further by 70 % by 2050 when compared to 2008, as a part of the Initial International Maritime Organization (IMO) Greenhouse Gas Strategy [5]. To follow this trend, it is essential to continuously improve and ensure the optimal performance and safety of LIBs. These tasks are handled by a Battery Management System (BMS), which among other things monitors important internal states of the battery cells within the battery packs. Failing this task may lead to serious consequences, such as thermal runaway [6].

Monitoring and controlling internal states such as State of Charge (SOC), State of Health (SOH), State of Power (SOP), and State of Energy (SOE) in LIBs is critical for ensuring safe operation [7]. These internal states cannot be measured directly, requiring a BMS to provide accurate state estimates in real-time based on measurements such as current, voltage, and temperature. This is a difficult task due to the time-varying and nonlinear nature of batteries, as well as their sensitivity to temperature and noise, making accurate modeling

difficult [8]. The SOC is a fundamental state to estimate accurately, because the other internal states, such as the ones mentioned above, are based on the SOC [4]. While methods like Coulomb counting, which directly measures the charge going in and out of the battery, do not rely on models, model-based estimation is more suitable for EV applications due to improved estimation accuracy and other advantages [9] [10]. Battery models can be classified into three categories: physics-based electrochemical models, Equivalent Circuit Models (ECMs), and data-driven models [8]. Of these, the ECMs possess the least complicated structure, easiest implementation, and lowest computational complexity, making them widely used. However, they are not able to extract hidden features inside the battery, which can be provided by for example an electrochemical model [4].

1.2 Previous work

SOC estimation using nonlinear ECMs has been extensively researched over recent years. In particular, different Kalman filter algorithms have been employed for model-based SOC estimation with overall good results [11]. Several studies in i.a. [12, 13, 14, 15] have investigated the performance of the Moving Horizon Estimator (MHE) relative to the Extended Kalman filter (EKF) and/or the Unscented Kalman filter (UKF), suggesting that the MHE is the superior estimator for SOC estimation accuracy as well as battery constraint handling capabilities. The specific choice of ECM and the cell chemistry it models is of significance for estimation accuracy. In [16] a comparative study on the performance of different ECMs employed for four different, commonly used LIB cell chemistries was conducted. It was concluded that a Thevenin (1RC) model offered a good balance between estimation accuracy and complexity for an NMC-type cell, whereas for an LFP-type cell, the 1RC model with a hysteresis element was the best option. The latter model is the same as the enhanced self-correcting (ESC) model used in this thesis.

1.3 Problem description

This master's thesis compares the SOC estimation performance of three different nonlinear state estimators using three ECMs, applied to two different LIB cell chemistries. The nonlinear estimators are namely the EKF, the Sigma-Point Kalman filter (SPKF), and the MHE. The variant of the SPKF implemented in this thesis is the Central Difference Kalman filter (CDKF), which is simply and mostly referred to as the SPKF throughout the thesis. The UKF is the other variant of the SPKF. The ECMs are the Rint (R), the 1RC, and ESC models. The two different battery cells are the NMC and LFP type cells, which among other things, have different open-circuit voltage characteristics, that are of great concern for model-based SOC estimation.

1.4 Delimitations

The scope of this thesis has been delimited to SOC estimation using ECMs only. Thus other internal states such SOH, SOP, and SOE, which are also important to monitor in

a BMS, have been disregarded. Other methods for SOC estimation such as data-driven methods are also not covered herein.

1.5 Contributions

The main contribution of this report is the comparison between the EKF, SPKF, and MHE for SOC estimation performance using the R, 1RC, and ESC models for both an NMC cell and an LFP cell. A side contribution is the investigation of the MHE SOC estimation performance using the ESC model.

1.6 Structure of the thesis

This thesis is divided into eight chapters, starting with the current, Chapter 1, as an introduction. Chapter 2 will provide the necessary theoretical foundation for understanding and performing state estimation of lithium-ion batteries, as well as theory relevant to the state estimators themselves. In Chapter 3, the focus will shift to the modeling of lithium-ion batteries. The state estimators used in conjunction with these models will be presented in Chapter 4. Chapter 5 will elaborate on the methodology of the work in the thesis, while the obtained results are presented in Chapter 6. The final two chapters, Chapter 7 and Chapter 8, are dedicated to a structured discussion and conclusion of these results, respectively.

2

Theory

This chapter presents the relevant theory of concepts and methods used in this thesis. The first section, Section 2.1, presents the relevant theory of LIBs. The main focus here is put on the concepts that are directly relevant to the understanding and intuition of state estimation of LIBs. Note that section is similar to the corresponding section in the specialization project written by the same author [17]. Section 2.2 proceeds with the theoretical basis for the Kalman filter algorithms used herein, and Section 2.3 presents theory around optimization problems that is relevant to the MHE. The last section, Section 2.4, presents nonlinear observability which forms the basis for a nonlinear observability analysis later in the thesis.

2.1 Lithium-ion batteries

2.1.1 Basic working principle

A lithium-ion battery can consist of a single lithium-ion cell or several interconnected lithium-ion cells, depending on its application. Here the basic working principle of a single lithium-ion cell is covered. A lithium-ion cell consists of four major elements: two electrodes: anode and cathode, a separator, and electrolyte [18]. These elements can be seen in the illustration of a lithium-ion cell during a discharge process in Figure 2.1.

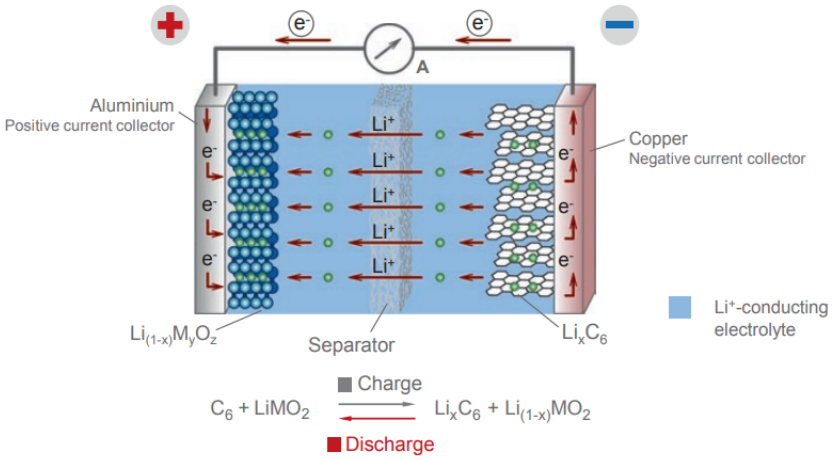

Figure 2.1: The setup of a LIB during a discharge process [19].

The anode consists of an active material, in which the lithium-ions intercalate and deintercalate, and a current collector. Here intercalation refers to the reversible process of lithium-ions being inserted in between the layers or voids of the crystalline structure of the active material in the electrodes during charging and discharging of the cell [20]. In LIBs, the anode active material is typically made of graphite and amorphous carbon compounds, whereas the anode current collector can consist of copper. The cathode typically has an active material of mixed oxides, and a current collector of for example aluminum. The two electrodes are surrounded with lithium-ion conducting electrolyte and are electrically isolated from each other by a separator. The separator allows for a flow of lithium ions between the electrodes, but not electrons. Thus by connecting the two electrodes together with an external conductive cable, a flow of electrons, or current, can occur [19].

During discharge, due to a difference in electrochemical potential energy between the electrodes creating an electromotive force, the favored reaction is that the active material in the anode releases lithium-ions into the electrolyte, and electrons into the external circuit via the current collectors. The resulting flow of electrons can be utilized to do useful work, e.g. powering a device. During charging, the mentioned reaction is reversed [21].

2.1.2 NMC and LFP type cells

Lithium-ion batteries can be based on different cell chemistries. Depending on which active material is used in the anode and cathode, changes to energy density and cost-effectiveness occur. Of relevance for this thesis are the NMC and LFP type cells, which consist of different cathode active materials. The Lithium Nickel Manganese Cobalt Oxide (NMC) cell has a layered cathode structure of $Li(Ni_xMn_yCo_z)O_2$ where the molar fractions (x, y, z) add up to one. The Lithium Iron Phosphate (LFP) cell has an olivine cathode structure made of iron phosphate ($FePO_4$) [16]. There are differences and varia-

tions within the cell types themselves, but in general, the LFP chemistry has lower cutoff voltages and a flatter open-circuit voltage behavior than the NMC chemistry. Also, LFP cells are inherently safer from thermal runaways and are cheaper to produce when compared to NMC cells. The NMC-type cells have a higher energy density, and both cell types offer long durability [22]. The chemical reaction equations for the two cell types can be seen in and Table 2.2, and the battery data for two specific cells that are used in this thesis can be seen in Table 5.1.

Electrode	Electrochemical Reactions
Anode	$Li_nC_6 \rightleftharpoons Li_0C_6 + nLi^+ + ne^-$
Cathode	$Li_{m-n}(Ni_xMn_yCo_z)O_2 + nLi^+ + ne^- \rightleftharpoons Li_m(Ni_xMn_yCo_z)O_2$
Overall	$Li_nC_6 + Li_{m-n}(Ni_xMn_yCo_z)O_2 \rightleftharpoons Li_0C_6 + Li_m(Ni_xMn_yCo_z)O_2$

Table 2.1: The chemical reaction equations for the NMC type cell [16].

Electrode	Electrochemical Reactions
Anode	$Li_nC_6 \rightleftharpoons Li_0C_6 + nLi^+ + ne^-$
Cathode	$Li_{m-n}FePO_4 + nLi^+ + ne^- \rightleftharpoons Li_mFePO_4$
Overall	$Li_nC_6 + Li_{m-n}FePO_4 \rightleftharpoons Li_0C_6 + Li_mFePO_4$

Table 2.2: The chemical reaction equations for the LFP type cell [16].

2.1.3 Capacity C

To orderly define other relevant and important internal states of the battery later in the report, a clear definition of a battery's capacity C is needed. The actual capacity C of a battery is the amount of electric charge that a fully charged battery can deliver under predetermined reference conditions and is given in units of ampere-hours (Ah). The fully charged and empty state of the battery is defined by the manufacturer. Due to aging of the battery during its lifetime, the actual capacity will continuously decrease from the *beginnng of life* (BOL) until its *end of life* (EOL) [23]. The specified capacity given by a manufacturer is termed the *nominal* or *rated* capacity and is denoted C_n. Hence in theory, at BOL for a fully charged battery, the actual capacity and nominal capacity of the battery are equal. For current rates, 1C is the relative measure of current that explains how much constant current is needed to completely discharge the battery in one hour [21].

2.1.4 State of Charge

The LIB's State of Charge can be defined as the ratio between the available capacity and the total available capacity of a fully charged battery under reference conditions. In short:

$$SOC = SOC(t) = \frac{q(t)}{C} \tag{2.1}$$

where q(t) is the available capacity, or equivalently, the stored electric charge in the battery at a given point in time [23]. The SOC is a unitless number in the range $[0 \quad 1]$ or $[0\% \quad 100\%]$, where 100 % SOC implies a fully charged battery and 0 % SOC implies a fully discharged battery [21]. Throughout the thesis, the SOC is also denoted by the letter z.

2.1.5 Open-circuit voltage

The battery's open-circuit voltage (OCV) is the voltage between the terminals of the battery when there is no battery current. In general, since stored electric charge $q(t)$ is dependent on time, and since the open-circuit voltage is dependent on the stored electric charge in the battery, the OCV(t) can also be seen as time-dependent. Since the SOC is dependent on $q(t)$, the OCV can be described as dependent on the SOC of the battery [23]. The latter relationship will be used in this report, and it is often a static function that is found experimentally in laboratories under specific conditions, such as constant temperature for instance [21]. For further reading, this relationship is described by the function $OCV(z(t))$, and referred to as the OCV-SOC relationship, or simply the OCV curve.

2.1.6 Polarization voltages

Polarization in lithium-ion batteries refers to the voltages that create a notable deviation in terminal voltage and open-circuit voltage due to a current running in or out of the cell [21]. There are several different polarization phenomena present in a LIB during charge and discharge cycles, and they all have in common that they cause loss of energy and decrease the efficiency of the cell. Typical forms of polarization are ohmic polarization, activation polarization, and concentration polarization. These occur in different parts of the cell, and their individual voltage contributions vary with the external cell excitation current [24]. In [25], the deviation is formulated as

$$V_{bat} - V_{OCV} = V_{ohmic} + V_{f,pos} + V_{f,neg} + V_{act,pos} + V_{act,neg} + V_{con} \tag{2.2}$$

where $V_{f,pos}$ and $V_{f,neg}$ represent the voltage drop due to passivation films or layers on the positive and negative electrodes, and $V_{f,act}$ and $V_{f,act}$ are voltage drops due to interfacial charge-transfer reactions at the electrodes. V_{con} adds the polarization obtained from phenomena such as lithium diffusion.

Ohmic polarization represents the general limitation in conductivity of ions and electrons in the current collectors, active materials, terminals, connectors, and electrolyte [25]. This can be modeled through Ohm's law with a resistor R_0 to indicate the near-instantaneous voltage drop that occurs when a battery current is passing through the cell, such that

$$V_{ohmic} = R_0 i_{bat} \tag{2.3}$$

where i_{bat} is the battery current [21].

Activation polarization occurs since the electrochemical reaction rate at the electrodes is lower than the electron velocity [26], This phenomena will not be elaborated or explored in any greater detail. Concentration polarization implies voltage drops due to effects such as diffusion, migration, and convection [25]. Of relevance for this report is the diffusion dynamics.

2.1.7 Warburg impedance

For alternating current excitations of batteries, the electrochemical interface of the battery shows resistance in terms of impedance. This can be modeled and explained with an equivalent circuit, namely the Randles circuit depicted in Figure 2.2.

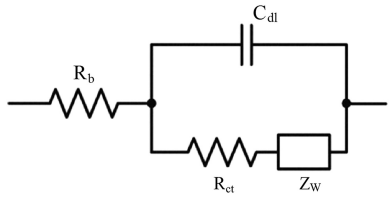

Figure 2.2: The Randles circuit [27].

The resistor R_b represents the bulk resistance of the cell, where the resistance in the ionic conductivity in the electrolyte, separator, and electrodes is considered. The resistor R_{ct} models the charge transfer resistance and the capacitor C_{dl} stands for the double-layer capacitance. These two in combination contribute to the activation polarization. The Warburg impedance element Z_w models the impedance due to the diffusion of lithium-ions in the cell [27], which is part of the concentration polarization. The Warburg impedance element may be described by

$$Z_w = \frac{A_w}{\sqrt{j\omega}} \tag{2.4}$$

where A_w is called the Warburg coefficient and frequency ω is given in $\frac{rad}{s}$. A Nyquist plot of the cell impedance is shown in Figure 2.3.

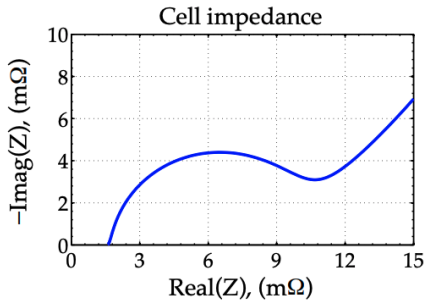

Figure 2.3: Nyquist plot of a realistic cell's electrochemical impedance spectrum (EIS). The utilized model here is the 1RC model found in Section 3.2. [21].

Here it can be observed that at low frequencies, a straight line of 45° appears in the EIS, which is due to the 45° phase shift that is contributed by the Warburg element to the cell. For the intermediate frequencies, the charge transfer dynamics are represented, which are modeled by the RC pair. At the intersection between the curve and the real axis, the impedance in the cell in the form of pure ohmic resistance R_b is found [21].

As there is no simple ordinary-differential equation for the dynamics of the Warburg impedance element, simulations using Randle's circuit becomes cumbersome. In order to model and simulate these dynamics, the Warburg element can be approximated by multiple resistor-capacitor subcircuits in series, as illustrated in Figure 2.4.

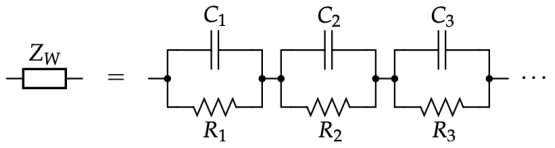

Figure 2.4: Approximation of the Warburg impedance element using RC subcircuits [21].

To be equivalent to the original Warburg element, an infinite number of RC subcircuits is required. However, over some frequency range, a reasonably small number of RC subcircuits can model the diffusion effects very well [21].

2.1.8 Hysteresis

The OCV, modeled as a voltage source, is present in most ECMs. The OCV as a function of the SOC is principal in model-based state estimation of LIBs. If the OCV-SOC relationship is well known, the SOC can be determined based on the OCV, under certain no-load conditions. However, this assumes a one-to-one relationship between the two, which is not the case if hysteresis is present [28]. In short, hysteresis in LIBs originates from entropic stress, mechanical stress, and microscopic distortions within the active materials in the

electrodes [29]. A consequence of this is that the cell relaxes to a different OCV depending on if the cell was last charging or discharging, which implies that there exist several possible open-circuit voltages for the same SOC. This can cause significant inaccuracy in SOC estimation. To improve on this accuracy, some knowledge of the charge-discharge history must be included in the modeling [28]. However, it is, in general, difficult to model hysteresis because it is not a phenomenon that is very well understood [21]. In Figure 2.5 a fully charged cell has first been discharged to 0 % SOC with a C/30 rate, and charged back up 95 % SOC with the same rate, then discharged to 5 % SOC, and so forth. The low C-rate ensures that the cell is very close to equilibrium rest voltage. As seen there exist several rest voltages per SOC, giving evidence to the presence of voltage hysteresis [21].

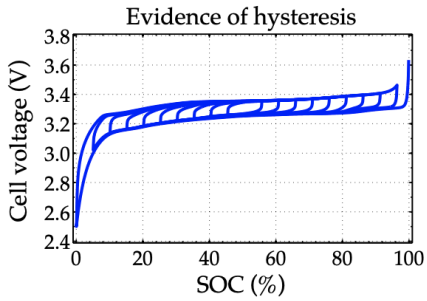

Figure 2.5: Evidence of hysteresis [21].

2.2 Sequential probabilistic inference

The sequential probabilistic inference problem tries to estimate a state (or parameter) of a system such that it minimizes the mean-squared error between the true state and the state estimate. In this process, all observed measurements of the input and output up until the current time step are taken into consideration when estimating the unknown state [30]. Consider the discrete-time state-space system on the form

$$\mathbf{x}_k = \mathbf{f}(\mathbf{x}_{k-1}, \mathbf{u}_{k-1}, \mathbf{w}_{k-1}) \tag{2.5}$$

$$\mathbf{y}_k = \mathbf{h}(\mathbf{x}_k, \mathbf{u}_k, \mathbf{v}_k) \tag{2.6}$$

where $\mathbf{x}_k \in \mathbb{R}^n$ is the state vector at time step k, $\mathbf{y}_k \in \mathbb{R}^m$ is the measurements and $\mathbf{u}_k \in \mathbb{R}^p$ is the input. Here (2.5) is the state equation representing the system dynamics, and (2.6) is the output equation representing the measurements. The stochastic variable $\mathbf{w}_k \in \mathbb{R}^n$ models unmeasured noise, disturbance, or uncertainty that affects the states of the system, and $\mathbf{v}_k \in \mathbb{R}^m$ is the stochastic variable that models sensor noise that impacts the measurements of the system in a memoryless way without directly impacting the states.

Since the stochastic noise variables directly affect the states and measurements, the state estimates and the observed measurements are not deterministic. Thus, through probabilistic inference one attempts to form an estimate of the system state given all observations $\mathbb{Y}_k = \{\mathbf{y}_0, \mathbf{y}_1, ..., \mathbf{y}_k\}$, which can be expressed with an estimator based on the conditional mean such that

$$\hat{\mathbf{x}}_k = \mathbb{E}\left[\mathbf{x}_k \mid \mathbb{Y}_k\right] = \int_{R_{\mathbf{x}_k}} \mathbf{x}_k p\left(\mathbf{x}_k \mid \mathbb{Y}_k\right) \mathrm{d}\mathbf{x}_k \tag{2.7}$$

where $R_{\mathbf{x}_k}$ is the set of valid $\mathbf{x}_k$. Finding the optimal solution to this problem requires the computation of the posterior probability density $p\left(\mathbf{x}_k \mid \mathbb{Y}_k\right)$, which is done recursively with two steps per iteration. These are namely the prediction and update steps. The prediction step yields a prediction of $\mathbf{x}_k$ given all previous observations by

$$p\left(\mathbf{x}_k \mid \mathbb{Y}_{k-1}\right) = \int_{R_{\mathbf{x}_{k-1}}} p\left(\mathbf{x}_k \mid \mathbf{x}_{k-1}\right) p\left(\mathbf{x}_{k-1} \mid \mathbb{Y}_{k-1}\right) \mathrm{d}\mathbf{x}_{k-1} \tag{2.8}$$

and the update step updates the prediction with the new measurement through

$$p\left(\mathbf{x}_k \mid \mathbb{Y}_k\right) = \frac{p\left(\mathbf{y}_k \mid \mathbf{x}_k\right) p\left(\mathbf{x}_k \mid \mathbb{Y}_{k-1}\right)}{p\left(\mathbf{y}_k \mid \mathbb{Y}_{k-1}\right)} \tag{2.9}$$

where Bayes' rule is applied. Note that it is assumed that observation $\mathbf{y}_k$ is conditionally independent of previous measurements given the state $\mathbf{x}_k$. The probabilities in (2.9) can be calculated as

$$p\left(\mathbf{y}_k \mid \mathbb{Y}_{k-1}\right) = \int_{R_{\mathbf{x}_k}} p\left(\mathbf{y}_k \mid \mathbf{x}_k\right) p\left(\mathbf{x}_k \mid \mathbb{Y}_{k-1}\right) \mathrm{d}\mathbf{x}_k \tag{2.10}$$

$$p\left(\mathbf{x}_k \mid \mathbf{x}_{k-1}\right) = \sum_{\{w:\mathbf{x}_k = f(\mathbf{x}_{k-1}, \mathbf{u}_{k-1}, w, k-1)\}} p(w) \tag{2.11}$$

$$p\left(\mathbf{y}_k \mid \mathbf{x}_k\right) = \sum_{\{v:\mathbf{y}_k = h(\mathbf{x}_k, \mathbf{u}_k, v, k)\}} p(v) \tag{2.12}$$

However, calculating these probabilities is not a trivial task, and is often unmanageable in real-time applications. If the system at hand allows the computational expense required, Monte Carlo methods such as *particle filters* approximate the multi-dimensional integrals above very accurately. However, in a BMS that governs tens or hundreds of battery cells, this solution is often economically infeasible.

If one assumes that all probability densities are Gaussian, a simplified solution can be made. This implies that rather than needing to propagate the entire density function through time, one only has to compute the conditional mean and variance of the states once each sampling time. This approximation is what forms the basis for the recursive algorithms of the EKF and the SPKF [31].

2.3 Optimization problem

2.3.1 Nonlinear programming

Nonlinear programming is the process of optimizing a nonlinear objective function in the presence of equality and inequality constraints, which may also be nonlinear. Generally, the nonlinear program (NLP) can be formulated in standard form as

$$\begin{aligned} \text{Minimize} \quad & f(\mathbf{x}) \\ \text{subject to} \quad & \mathbf{g}_i(\mathbf{x}) \leq 0 \quad \text{for } i = 1, ..., m \\ & \mathbf{h}_i(\mathbf{x}) = 0 \quad \text{for } i = 1, ..., l \\ & \mathbf{x} \in X \end{aligned} \tag{2.13}$$

where f is a single-valued objective function and $\mathbf{x} = [\mathbf{x}_1, ..., \mathbf{x}_n]^T$ is a vector of n components, often referred to as *optimization variables* or *decision variables*. That is, these are the variables that need to minimize the objective function subject to the inequality constraints $\mathbf{g}(\mathbf{x})$ and equality constraints $\mathbf{h}(\mathbf{x})$, while also being contained within the set X. This set typically includes upper and lower bounds on the optimization variables. A vector $\mathbf{x}$ that satisfies all these constraints, is called a *feasible solution* to the problem. The domain of these solutions is termed the *feasible region*, and thus the objective is to find the optimal feasible solution [32]. Note that an NLP can have several optimal solutions, such that there may exist a global optimum and/or one or more local optimums inside the feasible region [33].

2.3.2 Optimal control problem

Optimization problems within control engineering are often formulated as finite horizon optimal control problems (OCPs), also for state estimation problems. In discrete time, a simple, general formulation can be set up as

$$\begin{aligned} \min_{\mathbf{x},\mathbf{u}} \quad & \sum_{k=0}^{N-1} L(\mathbf{x}_k, \mathbf{u}_k) + E(\mathbf{x}_N) \\ s.t. \quad & \mathbf{x}_{k+1} = \mathbf{f}(\mathbf{x}_k, \mathbf{u}_k); \quad k = 0, ..., N-1 \\ & \mathbf{x}_0 = \bar{\mathbf{x}}_0 \\ & \mathbf{u}_k \in U, \quad k = 0, ..., N-1 \\ & \mathbf{x}_k \in X, \quad k = 0, ..., N \end{aligned} \tag{2.14}$$

where the optimization variables $\mathbf{x}$ and $\mathbf{u}$ are found such that they minimize the cost function L as well as a terminal term E, subject to the given constraints over the horizon N. Note that the system dynamics, given by the function $\mathbf{f}(\mathbf{x}_k, \mathbf{u}_k)$, is included as an equality

constraint. The OCP is often nonlinear due to the nature of the system that is meant to be optimized [33, 34, 35].

2.3.3 Simultanous vs sequential approach

The OCP in (2.14) has both states and control input as optimization variables, and can therefore be constructed as a large and structured NLP in standard form that can readily be solved by an NLP solver. This approach is termed the simultaneous approach since the NLP solver has to solve both the simulation problem and the optimization problem simultaneously. For most NLP solvers, the model as an equality constraint will only be satisfied once the NLP iterations have converged. The OCP in (2.14) can be reduced to only having the control input $\mathbf{u}$ as an optimization variable, reducing the variable space compared to the original problem. As a consequence, the simulation problem and optimization problem are solved sequentially, which is why this approach is termed the sequential approach. Simultaneous methods include *direct multiple shooting* and *direct collocation*, whereas a sequential method is *direct single shooting*. When based on Newton-type optimization, simultaneous approaches typically offer faster local convergence rates when compared to a sequential approach, in particular for unstable or highly nonlinear systems [35, 36]. In this thesis, multiple shooting is utilized.

2.4 Nonlinear observability

When performing state estimation using a state space model, it is necessary that the model is observable. For linear time-invariant state space models, it is well-known that if the observability matrix has full rank, then the system states are observable. However, for nonlinear models, observability is not as straightforward [37].

2.4.1 Distinguishability and observability

Consider the nonlinear state space model

$$\dot{\mathbf{x}} = \mathbf{f}(\mathbf{x}) + \sum_{i=1}^{m} u_i \mathbf{g}_i(\mathbf{x}) \tag{2.15a}$$

$$\mathbf{y} = \mathbf{h}(\mathbf{x}) \tag{2.15b}$$

where $\mathbf{x} \in X$ is the state and X is an open subset of $\mathbb{R}^n$, $u_i \in \mathbb{R}$ is the input, and $\mathbf{y} \in \mathbb{R}^p$ is the output. Further, $\mathbf{f} : X \to \mathbb{R}^n$, $g_i : X \to \mathbb{R}^n$ and $\mathbf{h} : X \to \mathbb{R}^p$ are smooth functions. The following definition is introduced [37]:

- Definition 1: Suppose the system in (5.1) has two states: $\mathbf{x}_1$ and $\mathbf{x}_2$, where the system output at time t with initial state $\mathbf{x}_i$ and input u is denoted as $\mathbf{y}(\mathbf{x}_i, u, t)$ for $i = 1, 2$. Then $\mathbf{x}_1$ and $\mathbf{x}_2$ are *distinguishable* if there exists an input function u such that $\mathbf{y}(\mathbf{x}_1, u, t) \neq \mathbf{y}(\mathbf{x}_2, u, t)$ for a finite t. The system (5.1) is *locally observable* at

$\mathbf{x}_1$ if there exists a neighborhood $\mathcal{N}$ of $\mathbf{x}_1$ such that the only state in $\mathcal{N}$ that is not distinguishable from $\mathbf{x}_1$ is $\mathbf{x}_1$ itself. The system is said to be locally observable if this holds for every $x \in X$.

For nonlinear systems, two states may be distinguishable even if $\mathbf{y}(\mathbf{x}_1, u, t) = \mathbf{y}(\mathbf{x}_2, u, t)$, in contrast to linear systems where the above definition holds. Thus it is, in general, more difficult to distinguish between two states in a nonlinear system, since finding an input function u that gives different output functions may be difficult. It is also worth noting that local observability for linear systems implies global observability, which is not the case for nonlinear systems.

2.4.2 Observability rank test

The observability of a nonlinear system can be checked by performing an observability rank test [37]. This involves calculating Lie-derivatives of the system and inspecting the rank of an observability matrix containing these derivatives. Let $\mathbf{h}(\mathbf{x}) = [h_1(\mathbf{x}), h_2(\mathbf{x}), ..., h_p(\mathbf{x}))]^T$ be a p-dimensional vector function on X, where the jth component $h_j(\mathbf{x})$ is a real-valued smooth function. Then the gradient of h_j is

$$\mathbf{d}h_j = \begin{bmatrix} \frac{\partial h_j}{\partial \mathbf{x}_1} & \frac{\partial h_j}{\partial \mathbf{x}_2} & \cdots & \frac{\partial h_j}{\partial \mathbf{x}_n} \end{bmatrix} \tag{2.16}$$

and the Lie-derivative of h_j with respect to $\mathbf{f}(\mathbf{x}) = [f_1(\mathbf{x}), f_2(\mathbf{x}), ..., f_n(\mathbf{x}))]^T$ is a real-valued function defined by

$$L_f h_j = \mathbf{d}h_j \cdot \mathbf{f} = \sum_{i=1}^{n} f_i \frac{\partial h_j}{\partial \mathbf{x}_i} \tag{2.17}$$

Here the zeroth-order Lie-derivative is defined as $L_f^0 h_j = h_j$, and the second-order Lie-derivative e.g. is defined as $L_f^2 h_j = L_f L_f h_j$. Then observability is given by

- Theorem 1: The system in (5.1) is locally observable at $\mathbf{x}_0 \in X$ if there are n linearly independent rows in the set

$$(\mathbf{d}L_{z_s}\ L_{z_{s-1}} \ ...\ L_{z_1} h_j)(\mathbf{x}_0) \tag{2.18}$$

  where $s \geq 0$, $z_k \in \{f, g_1, ..., g_m\}$ for $k = 1, ..., s$ and $j = 1, ..., p$. If $s = 0$ the expression is defined as $\mathbf{d}h_j(\mathbf{x}_0)$.

It is important to note that this is a sufficient condition, but not a necessary condition for system (5.1) to be locally observable. Another important thing to note is that an observability analysis of the linearization around $\mathbf{x}_0$ of (5.1) may suggest that the system is unobservable at $\mathbf{x}_0$, whereas an application of Theorem 1 confirms observability [37]. Thus the observability of the linearized system is not a necessary condition for the nonlinear system to be locally observable.

3

Modeling of battery cells

In this chapter modeling of battery cells is presented [17]. All models that will be presented here are equivalent-circuit models and are represented by circuit diagrams, as can be seen in the following sections. The circuit dynamics is meant to approximate the behavior of a battery cell with regards to how voltage responds to different input currents [21]. For all the models both the continuous-time differential equations as well as the discrete-time difference equations will be given. This is because these models are intended for use in a discrete computer system in a BMS for real-time applications, but also because they are applied with the discrete-time algorithms of the Kalman filters.

3.1 The Rint model

One of the simplest Equivalent-Circuit models is the Rint (R) model [21, 38], which is represented by the circuit diagram shown in Figure 3.1. The ideal voltage source models the open-circuit voltage of the battery, which is a static function of the SOC, $z(t)$. The resistor R_0 tries to model the behavior of the cell in terms of resistance, and $i(t)$ is the load current defined as positive in its shown direction. This direction of load current implies a discharge of the battery cell.

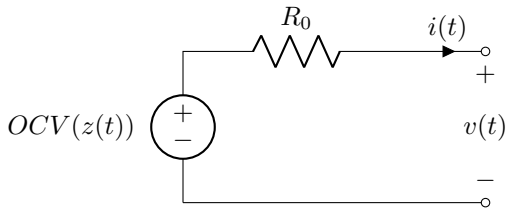

Figure 3.1: The Rint ECM.

The behavior of this model in continuous time can be described by

$$\dot{z}(t) = -\eta(t)\frac{i(t)}{Q} \tag{3.1}$$

$$v(t) = OCV(z(t)) - R_0 i(t) \tag{3.2}$$

or in discrete-time as

$$z_{k+1} = z_k - \frac{\Delta t}{Q}\eta_k i_k \tag{3.3}$$

$$v_k = OCV(z_k) - R_0 i_k \tag{3.4}$$

where $\eta(t)$ is the coulombic efficiency and Q is the actual capacity in units ampere-seconds As. Throughout the thesis, the coulombic efficiency is assumed to be 1.

3.2 The Thevenin model

Another popular ECM is the Thevenin (1RC) model [38][21], illustrated in the circuit diagram in Figure 3.2. The difference from the Rint model is that an RC subcircuit has been added, in order to model the slow diffusion process of lithium-ions in the battery cell. These voltages are referred to as diffusion voltages.

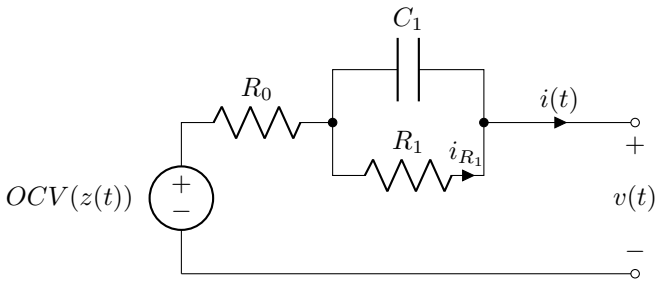

Figure 3.2: The Thevenin ECM.

The dynamics of the model may be described by

$$\dot{z}(t) = -\eta(t)\frac{i(t)}{Q} \tag{3.5}$$

$$\dot{i}_{R_1}(t) = -\frac{1}{R_1 C_1} i_{R_1}(t) + \frac{1}{R_1 C_1} i(t) \tag{3.6}$$

$$v(t) = OCV(z(t)) - R_1 i_{R_1}(t) - R_0 i(t) \tag{3.7}$$

or in discrete time

$$z_{k+1} = z_k - \frac{\Delta t}{Q}\eta_k i_k \tag{3.8}$$

$$i_{R_1,k+1} = \exp\left(\frac{\Delta t}{R_1 C_1}\right) i_{R_1,k} + \exp\left(1 - \frac{\Delta t}{R_1 C_1}\right) i_k \tag{3.9}$$

$$v_k = OCV(z_k) - R_1 i_{R_1,k} - R_0 i_k \tag{3.10}$$

3.3 The enhanced self-correcting model

A slightly more advanced ECM compared to the preceding models, namely the enhanced self-correcting (ESC) model [21], can be observed in Figure 3.3. In addition to the elements found in the previous models, the ESC model also contains a nonlinear *hysteresis* element to account for voltage hysteresis in the battery cell.

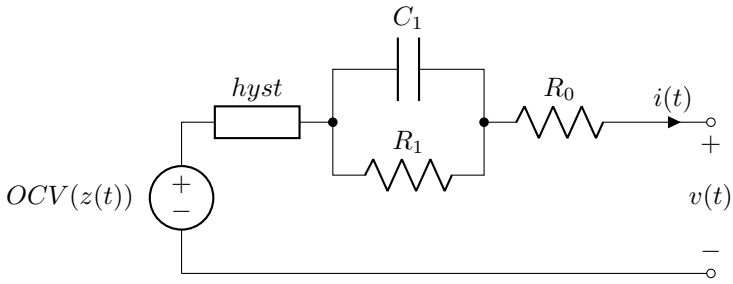

Figure 3.3: The enhanced self-correcting ECM.

Here a nonlinear time-varying system, as proposed in [21], is used to model hysteresis $h(t)$ somewhat simplified. The differential equation of the element is given by

$$\dot{h}(t) = -\left|\frac{\eta(t) i(t) \gamma}{Q}\right| h(t) + \left|\frac{\eta(t) i(t) \gamma}{Q}\right| M(z, \dot{z}) \tag{3.11}$$

whereas in discrete-time the difference equation when using the simple representation $M(z, \dot{z}) = sgn(i_k)$ becomes

$$h_{k+1} = \exp\left(-\left|\frac{\eta_k i_k \gamma \Delta t}{Q}\right|\right) h_k + \left(\exp\left(-\left|\frac{\eta_k i_k \gamma \Delta t}{Q}\right|\right) - 1\right) sgn(i_k) \tag{3.12}$$

where in addition to the previously defined parameters, $\gamma > 0$ tunes the rate of decay for the hysteresis voltage. The state h_k accounts for dynamic hysteresis. By also adding a memory variable s_k, instantaneous hysteresis is accounted for in the measurement equation. Let

$$s_k = \begin{cases} sgn(i_k), & |i_k| > 0 \\ s_{k-1} & \text{otherwise} \end{cases} \tag{3.13}$$

The full model is represented by

$$z_{k+1} = z_k - \frac{\Delta t}{Q}\eta_k i_k \tag{3.14}$$

$$i_{R_1,k+1} = \exp\left(\frac{\Delta t}{R_1 C_1}\right) i_{R_1,k} + \exp\left(1 - \frac{\Delta t}{R_1 C_1}\right) i_k \tag{3.15}$$

$$h_{k+1} = \exp\left(-\left|\frac{\eta_k i_k \gamma \Delta t}{Q}\right|\right) h_k + \left(\exp\left(-\left|\frac{\eta_k i_k \gamma \Delta t}{Q}\right|\right) - 1\right) sgn(i_k) \tag{3.16}$$

$$v_k = OCV(z_k) + Mh_k + M_0 s_k - R_1 i_{R_1,k} - R_0 i_k \tag{3.17}$$

4

Nonlinear State estimation

4.1 Extended Kalman filter

In this section, the *extended Kalman filter* (EKF) is presented, which applies to nonlinear systems [17]. Recall the general form of a discrete-time nonlinear system

$$\begin{aligned} \mathbf{x}_{k+1} &= \mathbf{f}(\mathbf{x}_k, \mathbf{u}_k, \mathbf{w}_k) \\ \mathbf{y}_k &= \mathbf{g}(\mathbf{x}_k, \mathbf{u}_k, \mathbf{v}_k) \end{aligned} \tag{4.1}$$

where additive Gaussian distributed process noise $\mathbf{w_k}$ measurement noise $\mathbf{v}_k$ is included in the model. The working principle of the EKF is similar to that of the linear Kalman filter in terms of prediction and correction steps, but due to the nonlinearities of the system, a linearization is performed each time step [30]. The EKF makes two simplifying assumptions in order to apply the sequential probabilistic inference equations to a nonlinear model. Firstly, the approximation $\mathbb{E}[\mathbf{f}(\mathbf{x})] \approx \mathbf{f}(\mathbb{E}[\mathbf{x}])$ is used, which essentially states that the expected value of a nonlinear function $\mathbf{f}$ evaluated at the unknown state $\mathbf{x}$ is approximately the same as the nonlinear function $\mathbf{f}$ evaluated in the expected value of the unknown state $\mathbf{x}$. This is strictly exact only for linear systems, and therefore the approximation becomes worse the more nonlinear the function $\mathbf{f}$ is. Secondly, when computing the covariance matrices, EKF only uses a first-order Taylor series expansion when linearizing the system around the current operating point, and truncates the higher-order terms. This is also a reason that the EKF performs better for systems with mild nonlinearities. The EKF algorithm based on [39] and [30] used here is summarized below.

Algorithm 1 The extended Kalman filter

Nonlinear state-space model:

$$\mathbf{x}_k = \mathbf{f}(\mathbf{x}_{k-1}, \mathbf{u}_{k-1}, \mathbf{w}_{k-1})$$
$$\mathbf{y}_k = \mathbf{g}(\mathbf{x}_k, \mathbf{u}_k, \mathbf{v}_k)$$

where $\mathbf{w}_k$ are $\mathbf{v}_k$ are independent samples from Gaussian distributions with means $\bar{w}$ and $\bar{v}$ and covariance matrices $\mathbf{\Sigma}_{\bar{\mathbf{w}}}$ and $\mathbf{\Sigma}_{\bar{\mathbf{v}}}$.

Define linearization:

$$\hat{\mathbf{A}}_k = \left.\frac{\partial \mathbf{f}(\mathbf{x}_k, \mathbf{u}_k, \mathbf{w}_k)}{\partial \mathbf{x}_k}\right|_{\mathbf{x}_k = \hat{\mathbf{x}}_k^+} \quad , \quad \hat{\mathbf{B}}_k = \left.\frac{\partial \mathbf{f}(\mathbf{x}_k, \mathbf{u}_k, \mathbf{w}_k)}{\partial \mathbf{w}_k}\right|_{\mathbf{w}_k = \bar{\mathbf{w}}_k}$$
$$\hat{\mathbf{C}}_k = \left.\frac{\partial \mathbf{g}(\mathbf{x}_k, \mathbf{u}_k, \mathbf{v}_k)}{\partial \mathbf{x}_k}\right|_{\mathbf{x}_k = \hat{\mathbf{x}}_k^-} \quad , \quad \hat{\mathbf{D}}_k = \left.\frac{\partial \mathbf{g}(\mathbf{x}_k, \mathbf{u}_k, \mathbf{v}_k)}{\partial \mathbf{v}_k}\right|_{\mathbf{v}_k = \bar{\mathbf{v}}_k}$$

Initialize: For k = 0

$$\hat{\mathbf{x}}_0^+ = \mathbb{E}[\mathbf{x}_0]$$
$$\mathbf{\Sigma}_{\tilde{\mathbf{x}},0}^+ = \mathbb{E}[(\mathbf{x}_0 - \hat{\mathbf{x}}_0^+)(\mathbf{x}_0 - \hat{\mathbf{x}}_0^+)^T]$$

Computation: For k = 1,2, ... end, calculate:

Prediction part

A priori estimate: $\hat{\mathbf{x}}_k^- = \mathbf{f}(\hat{\mathbf{x}}_{k-1}^+, \mathbf{u}_{k-1}, \bar{\mathbf{w}}_{k-1})$

A priori state error-covariance matrix: $\mathbf{\Sigma}_{\tilde{\mathbf{x}},k}^- = \hat{\mathbf{A}}_{k-1}\mathbf{\Sigma}_{\tilde{\mathbf{x}},k-1}^+\hat{\mathbf{A}}_{k-1}^T + \hat{\mathbf{B}}_{k-1}\mathbf{\Sigma}_{\tilde{\mathbf{w}}}\hat{\mathbf{B}}_{k-1}^T$

Output estimate: $\hat{\mathbf{y}}_k^- = \mathbf{g}(\hat{\mathbf{x}}_k^-, \mathbf{u}_k, \bar{\mathbf{v}}_k)$

Correction part

Kalman gain matrix: $\mathbf{L}_k = \mathbf{\Sigma}_{\tilde{\mathbf{x}},k}^-\hat{\mathbf{C}}_k^T[\underbrace{\hat{\mathbf{C}}_k\mathbf{\Sigma}_{\tilde{\mathbf{x}},k}^-\hat{\mathbf{C}}_k^T + \hat{\mathbf{D}}_k\mathbf{\Sigma}_{\bar{\mathbf{v}}}\hat{\mathbf{D}}_k^T}_{\approx\mathbf{\Sigma}_{\tilde{\mathbf{y}},k}}]^{-1}$

A posteriori estimate: $\hat{\mathbf{x}}_k^+ = \mathbf{A}\hat{\mathbf{x}}_k^- + \mathbf{L}_k(\mathbf{y}_k - \hat{\mathbf{y}}_k)$

A posteriori state error-covariance matrix: $\mathbf{\Sigma}_{\tilde{\mathbf{x}},k}^+ = \Sigma_{\tilde{\mathbf{x}},k}^- - \mathbf{L}_k\mathbf{\Sigma}_{\tilde{\mathbf{y}},k}\mathbf{L}_k^T$

4.2 Sigma-Point Kalman filter

The simplifying assumptions in the EKF causes reduced estimation accuracy for highly nonlinear systems, which merits the use of the Sigma-Point Kalman filter (SPKF) [17, 40]. The SPKF substitutes local linearization with evaluation of the statistical distribution of the nonlinear system output by deterministic sampling [41]. More specifically the SPKF estimates the mean and variance of the outputs of a nonlinear function using a small, fixed set of function evaluations called *sigma-points*. For this purpose, a set of input sigma-points are carefully chosen such that the mean and covariance of the input points coincide with the mean $\bar{\mathbf{x}}$ and the covariance $\mathbf{\Sigma}_{\bar{\mathbf{x}}}$ of the random variable that is normally used as input to the nonlinear function. The input sigma-points are then propagated through the nonlinear function individually, yielding a transformed set of output sigma-points [30]. This transformation of sigma-points is referred to as the *unscented* transform [42]. In Figure 4.1 the difference between the actual sampling of the mean and variance of a transformed random variable $\mathbf{x}$ is shown and compared to that of the EKF and SPKF transformations. Notice how accurate the SPKF transformation is compared to the EKF transformation.

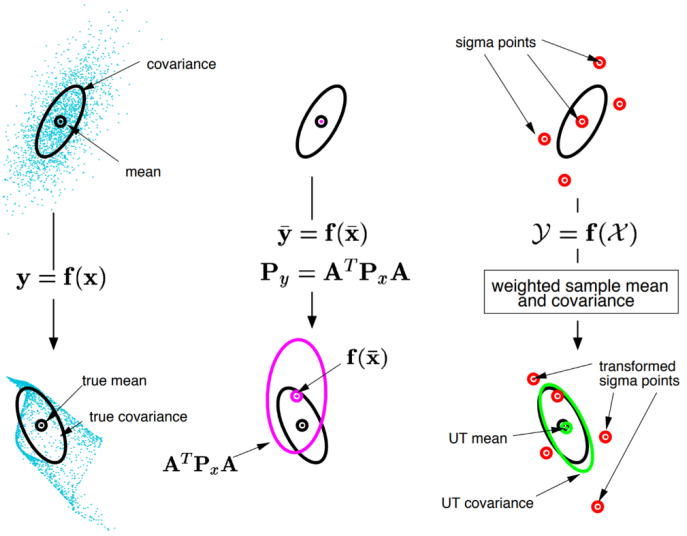

Figure 4.1: Illustration of the difference between actual sampling, linearized EKF transformation and the SPKF uscented transformation, in that order [42].

For details of how the different steps in the algorithm is derived, consult [30] for a comprehensive deduction. For the purpose of reasonable simplicity, a summary based on the same reference is provided below. As mentioned in the introduction, the SPKF comes in two variants, namely the CDKF and the UKF. The CDKF is implemented in this thesis and is mainly just referred to as the SPKF.

Algorithm 2 The Sigma-Point Kalman filter

Nonlinear state-space model:

$$\mathbf{x}_k = \mathbf{f}(\mathbf{x}_{k-1}, \mathbf{u}_{k-1}, \mathbf{w}_{k-1})$$
$$\mathbf{y}_k = \mathbf{g}(\mathbf{x}_k, \mathbf{u}_k, \mathbf{v}_k)$$

where $\mathbf{w}_k$ are $\mathbf{v}_k$ are independent samples from Gaussian distributions with means $\bar{w}$ and $\bar{v}$ and covariance matrices $\mathbf{\Sigma}_{\bar{\mathbf{w}}}$ and $\mathbf{\Sigma}_{\bar{\mathbf{v}}}$.

Define:

$$\mathbf{x}_k^a = [\mathbf{x}_k^T, \mathbf{w}_k^T, \mathbf{v}_k^T]^T, \quad \mathcal{X}_k^a = [(\mathcal{X}_k^x)^T,\ (\mathcal{X}_k^w)^T,\ (\mathcal{X}_k^v)^T]^T \ \text{(sigma-points)}$$
$$p = 2 \times \dim(\mathbf{x}_k^a)$$

Initialize: For k = 0

$$\hat{\mathbf{x}}_0^+ = \mathbb{E}[\mathbf{x}_0], \quad \mathbf{\Sigma}_{\tilde{\mathbf{x}},0}^+ = \mathbb{E}[(\mathbf{x}_0 - \hat{\mathbf{x}}_0^+)(\mathbf{x}_0 - \hat{\mathbf{x}}_0^+)^T]$$
$$\hat{\mathbf{x}}_0^{a,+} = \mathbb{E}[\mathbf{x}_0^a] = [(\hat{\mathbf{x}}_0^+)^T, \bar{\mathbf{w}}, \bar{\mathbf{v}}]^T$$
$$\mathbf{\Sigma}_{\tilde{\mathbf{x}},0}^{a,+} = \mathbb{E}[(\mathbf{x}_0^a - \hat{\mathbf{x}}_0^{a,+})(\mathbf{x}_0^a - \hat{\mathbf{x}}_0^{a,+})^T] = \mathit{diag}(\mathbf{\Sigma}_{\tilde{\mathbf{x}},0}^+, \mathbf{\Sigma}_{\tilde{\mathbf{w}}}, \mathbf{\Sigma}_{\tilde{\mathbf{v}}})$$

Computation: For k = 1,2, ... end, calculate:

Prediction part

A priori estimate:

$$\mathcal{X}_{k-1}^{a,+} = \left\{ \hat{\mathbf{x}}_{k-1}^{a,+}, \quad \hat{\mathbf{x}}_{k-1}^{a,+} + \gamma\sqrt{\Sigma_{\tilde{x},k-1}^{a,+}}, \quad \hat{\mathbf{x}}_{k-1}^{a,+} - \gamma\sqrt{\Sigma_{\tilde{x},k-1}^{a,+}} \right\}$$
$$\mathcal{X}_{k,i}^{x,-} = \boldsymbol{f}\left(\mathcal{X}_{k-1,i'}^{x,+}\mathbf{u}_{k-1}, \mathcal{X}_{k-1,i}^{w,+}\right)$$
$$\hat{\boldsymbol{x}}_k^- = \sum_{i=0}^{p} \alpha_i^{(\mathrm{m})} \mathcal{X}_{k,i}^{x,-}$$

A priori state error-covariance matrix:

$$\widetilde{\mathcal{X}}_{k,i}^{x,-} = \mathcal{X}_{k,i}^{x,-} - \hat{\mathbf{x}}_k^-$$
$$\mathbf{\Sigma}_{\tilde{\boldsymbol{x}},k}^- = \sum_{i=0}^{p} \alpha_i^{(\mathrm{c})} \left(\widetilde{\mathcal{X}}_{k,i}^{x,-}\right)\left(\widetilde{\mathcal{X}}_{k,i}^{x,-}\right)^T$$

Output estimate:

$$\mathcal{Y}_{k,i} = \boldsymbol{h}\left(\mathcal{X}_{k,i}^{x,-}, \boldsymbol{u}_k, \mathcal{X}_{k-1,i}^{v,+}\right)$$
$$\hat{\boldsymbol{y}}_k = \sum_{i=0}^{p} \alpha_i^{(\mathrm{m})} \mathcal{Y}_{k,i}$$

Correction part

Kalman gain matrix:

$$\tilde{\mathcal{Y}}_{k,i} = \mathcal{Y}_{k,i} - \hat{\mathbf{y}}_k$$
$$\boldsymbol{\Sigma}_{\tilde{y},k} = \sum_{i=0}^{p} \alpha_i^{(\mathrm{c})} \left(\tilde{\mathcal{Y}}_{k,i}\right)\left(\tilde{\mathcal{Y}}_{k,i}\right)^T$$
$$\boldsymbol{\Sigma}_{\tilde{x}\tilde{x},k}^{-} = \sum_{i=0}^{p} \alpha_i^{(\mathrm{c})} \left(\tilde{\mathcal{X}}_{k,i}^{x,-}\right)\left(\tilde{\mathcal{Y}}_{k,i}\right)^T$$
$$\mathbf{L_k} = \boldsymbol{\Sigma}_{\tilde{x}\bar{y},k}^{-} \boldsymbol{\Sigma}_{\tilde{y},k}^{-1}$$

A posteriori estimate:

$$\hat{\mathbf{x}}_k^{+} = \mathbf{A}\hat{\mathbf{x}}_k^{-} + \mathbf{L}_k(\mathbf{y}_k - \hat{\mathbf{y}}_k)$$

A posteriori state error-covariance matrix:

$$\boldsymbol{\Sigma}_{\tilde{\mathbf{x}},k}^{+} = \boldsymbol{\Sigma}_{\tilde{\mathbf{x}},k}^{-} - \mathbf{L}_k \boldsymbol{\Sigma}_{\tilde{\mathbf{y}},k} \mathbf{L}_k^T$$

4.3 Moving Horizon Estimator

The Moving Horizon Estimator (MHE) is a powerful state estimator that has obtained increasing success over recent years. The MHE takes into consideration a series of noisy measurements over a fixed horizon N backward in time and solves an optimization problem that yields an optimal state estimate each time step k. The optimization problem can be formulated as a linear, quadratic, or nonlinear program with constraints, implying that the MHE is able to handle both linear and nonlinear systems as well as system constraints during state estimation. Obtaining the solution to the optimization problem requires the use of a mathematical programming solver for each iteration, which can be a computationally expensive task [17, 43].

Consider again the general nonlinear discrete-time system on the form

$$\begin{aligned} \mathbf{x}_{k+1} &= \mathbf{f}(\mathbf{x}_k, \mathbf{u}_k, \mathbf{w}_k) \\ \mathbf{y}_k &= \mathbf{g}(\mathbf{x}_k, \mathbf{u}_k, \mathbf{v}_k) \end{aligned} \tag{4.2}$$

From a probabilistic point of view, the state estimation problem can be expressed as a discrete-time Markov process [44] [13]. This is equivalent to assuming that the process noise $\mathbf{w}_k$ is independent. Since the measurements are correlated with the states, the goal is to find the conditional probability density function of the state evolution $\{\mathbf{x}_0, \mathbf{x}_1, ..., \mathbf{x}_k\}$ given the measurements $\{\mathbf{y}_0, \mathbf{y}_1, ..., \mathbf{y}_k\}$, i.e.

$$p\left(\mathbf{x}_0, \mathbf{x}_1, ..., \mathbf{x}_k \mid \mathbf{y}_0, \mathbf{y}_1, ..., \mathbf{y}_k\right) \tag{4.3}$$

such that the optimal state estimates $\{\hat{\mathbf{x}}_i\}_{i=0}^{k}$ can be found by the maximum *a posteriori* Bayesian (MAP) estimate

$$\{\hat{\mathbf{x}}_i\}_{i=0}^{k} = \arg\max_{\mathbf{x}} p\left(\mathbf{x}_0, \mathbf{x}_1, ..., \mathbf{x}_k \mid \mathbf{y}_0, \mathbf{y}_1, ..., \mathbf{y}_k\right) \tag{4.4}$$

By making the following simplifying assumptions

1. The disturbances $\mathbf{w}_k$ are mutually independent
2. $\mathbf{f}(\mathbf{x}_k, \mathbf{u}_k, \mathbf{w}_k) = \mathbf{f}(\mathbf{x}_k, \mathbf{u}_k) + \mathbf{w}_k$
3. The probability density functions of $\mathbf{w}_k$ and $\mathbf{v}_k$ are Gaussian with zero mean and variances Q and R respectively.
4. The probability density function of $\mathbf{x}_0$ is Gaussian with mean $\bar{\mathbf{x}}$ and variance $\mathbf{P}_0$

the solution to (4.4) can be stated as

$$\begin{aligned} \arg\min_{\mathbf{x}} = \|\hat{\mathbf{x}}_0 - \bar{\mathbf{x}}_0\|^2_{P_0^{-1}} + \sum_{i=0}^{k} \|y_i - \mathbf{g}(\mathbf{x}_i, \mathbf{u}_i)\|^2_{R^{-1}} \\ \sum_{i=0}^{k-1} \|\mathbf{x}_{k+1} - \mathbf{f}(\mathbf{x}_i, \mathbf{u}_i)\|^2_{Q^{-1}} \end{aligned} \tag{4.5}$$

which is defined as the *full information estimation* problem (FIE). Notice that this problem increases in size as new measurements are received, which is computationally infeasible in practical applications [14]. Thus, by introducing constraints to the problem, as well as setting a fixed horizon of the N last measurements, a nonlinear optimization problem over a fixed horizon backward in time can be formulated. This forms the MHE. In general, the MHE can be implemented by solving a nonlinear program (NLP) each time step k on the form

$$
\begin{aligned}
\min_{\mathbf{x}_{k-N},\{\hat{\mathbf{w}}_i\}_{i=0}^{k}} &= \|\hat{\mathbf{x}}_{k-N} - \bar{\mathbf{x}}_{k-N}\|^2_{P^{-1}_{k-N}} + \sum_{i=k-N}^{k} \|\mathbf{v}_i\|^2_{R^{-1}} \\
&\quad + \sum_{i=k-N}^{k-1} \|\mathbf{w}_i\|^2_{Q^{-1}} \\
&\quad s.t. \\
\mathbf{x}_{i+1} &= \mathbf{f}(\mathbf{x}_i, \mathbf{u}_i) + \mathbf{w}_i, \quad i = k-N, ..., N-1 \\
\mathbf{y}_i &= \mathbf{g}(\mathbf{x}_i, \mathbf{u}_i) + \mathbf{v}_i, \quad i = k-N, ..., N \\
\mathbf{w}_i &\in \mathbb{W}_i, \quad \mathbf{x}_i \in \mathbb{X}_i
\end{aligned}
\tag{4.6}
$$

where the solution to the NLP yields the optimal state estimates $\{\hat{\mathbf{x}}_i\}_{i=k-N}^{k}$ and disturbance estimates $\{\hat{\mathbf{w}}_i\}_{i=k-N}^{k}$ over the horizon N. Thus the optimal state estimate at time step k is the last element in the solution, denoted $\hat{\mathbf{x}}_k$. The second and third term in the cost function above is penalized with the inverse constant weighting matrices $\mathbf{Q}$ and $\mathbf{R}$, which represents the covariance of the process and measurement noise respectively. Moreover, these matrices represent the confidence in the model and measurements respectively. If $\mathbf{Q}$ is small relative to $\mathbf{R}$, then the model is trusted more than the measurements, and vice versa. Along with the horizon length N, these matrices are considered tuning parameters for the MHE.

The first term in the cost function is the *arrival cost*. This cost is an approximation that takes into account the information received up until $i = k - N$, i.e. prior to the start of the current estimation horizon. Here the deviation between the initial estimate $\hat{\mathbf{x}}_{k-N}$ in the current horizon and the a priori estimate $\bar{\mathbf{x}}_{k-N}$ is penalized with the inverse covariance matrix $\mathbf{P}^{-1}_{k-N}$ of the a priori estimate. The a priori estimate in the current horizon is the optimal estimate computed at $k - N$ time steps back. The covariance matrix $\mathbf{P}_{k-N}$ represents the confidence in the initial estimate in the horizon and is typically updated via the EKF state error covariance updates, and stored for use N timesteps later.

5

Methodology

5.1 Dataset

For model fitting and estimator performance evaluation, an open online battery dataset was used [45] [46]. The dataset is provided by the Center for Advanced Life Cycle Engineering (CALCE) group at the University of Maryland, and contain both OCV measurements as well as dynamic load current profiles for several different cell chemistries at different ambient temperatures. In this thesis the OCV measurements and load profiles for the INR 18650-20R (NMC) and the A123 (LFP) cylindrical type cells at an ambient temperature of 25 °C were used. The specifications for the two cell types can be seen in Table 5.1.

Type	Nominal voltage	Nominal capacity	Upper/lower cut-off voltage	Max. current	Operating temperature
INR 18650-20R	3.6 V	2.0 Ah	4.2 V/2.5 V	22 A	0-50 °C
A123	3.3 V	1.1 Ah	3.6 V/2.0 V	30 A	-30-50 °C [47]

Table 5.1: LIB cell specifications.

5.1.1 OCV-SOC tests

In [45] and [46], they measured the static OCV-SOC relationship of the two cell types by performing a low current OCV-SOC test on each cell. The first step of this test involved charging the cell with a 1C rate until it reached its upper cut-off voltage and a reduction in current to around 0.01C. The cell was thereafter fully discharged with a low current of C/20 to its lower cut-off voltage, before fully charging the cell again at the same rate until the upper cut-off voltage was reached. The full test for the two cell types can be seen in

Figure 5.1 and Figure 5.2. Note that measured temperature data was only available for the LFP cell.

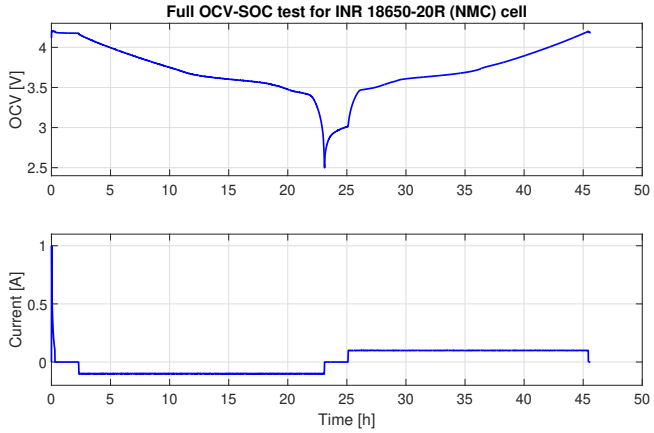

Figure 5.1: Full OCV-SOC test for the INR 18650-20R (NMC) cell conducted at an ambient temperature of 25 °C.

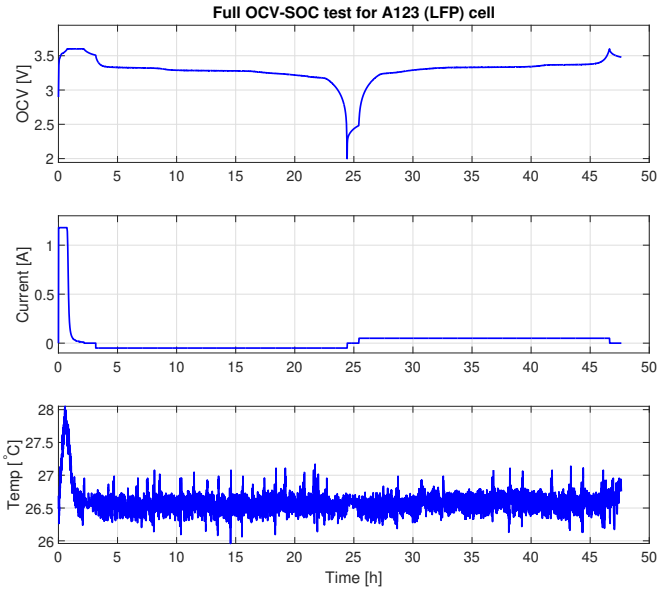

Figure 5.2: Full OCV-SOC test for the A123 (LFP) cell conducted at an ambient temperature of 25 °C.

From the resulting voltage measurements and the accumulated measured discharge and charge ampere-hours, both a charge and discharge OCV curve as a function of the SOC could be derived. Note that this requires the appropriate conversion of accumulated ampere-hours to SOC, such that the lower and upper cut-off voltages correspond to the open-circuit voltage of the cell at 0% SOC and 100% SOC, respectively. The reason for using a low charge and discharge current was to avoid exciting the dynamic parts of the cell, i.e. to minimize the effects of ohmic and diffusion polarization. Also, each test was performed at a constant ambient temperature, where heat generation caused by ohmic resistance in the cells is negligible due to low current [21].

It should be mentioned that in reality, some ohmic polarization and hysteresis are present during these tests, which cause the charge and discharge OCV curves to be somewhat different from one another. The average of the two curves can be used as the approximate static OCV-SOC curve in state estimators.

5.1.2 Load current profiles

The CALCE battery dataset contains several load current profiles with corresponding voltage measurements for the NMC and LFP cells. The ones used in this thesis are namely the Dynamic Stress Test (DST), the Federal Urban Driving Schedule (FUDS), and the US Highway 06 (US06) load profiles, and one cycle of each profile can be seen in Figure 5.3. The DST is designed by the US Advanced Battery Consortium (USABC), and it simulates the expected demands of an EV battery. The FUDS and US06 are also dynamic load current profiles, but they are more complex than the DST in regards to the charge/discharge rate of the current and are based on the time-velocity profile of an industry-standard EV [45] [46]. The FUDS cycle simulates urban driving, and the US06 simulates highway driving [48]. Note that these load profiles are scaled to fit each relevant cell. In the experimentation conducted in this thesis, the DST was used as input for parameter identification of the models presented in Chapter 3, whereas the FUDS and US06 were used as input for estimator performance evaluation. This is the same approach taken in the research papers that have used the same data, referenced earlier in this section [45] [46].

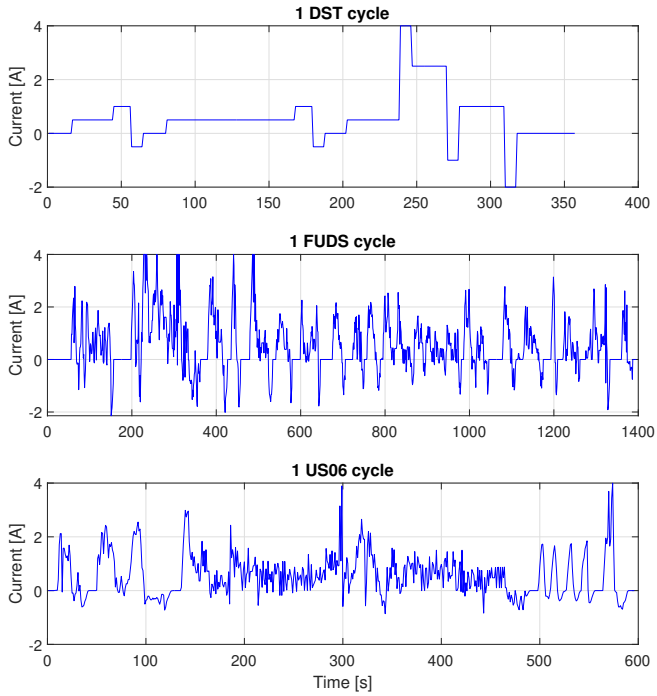

Figure 5.3: The load current profiles in the CALCE dataset for the NMC cell at an ambient temperature of 25 °C.

5.2 OCV-SOC relationship

5.2.1 OCV-SOC curve approximation

The final charge, discharge, and average OCV curves for the two cell types were established by using the parts of the OCV-SOC tests above where only a low current was applied. This was done to avoid including the parts of the curve that results from slow lithium diffusion rather than an imposed current and consequently a change in SOC. The reference SOC was determined by the measured accumulated discharge ampere-hours at each time step divided by the total capacity of the cell. Here the discharge capacity of the cell was the measured discharge capacity during the low current OCV-SOC test, which was $Q = 2.0802$ Ah for the NMC cell and $Q = 1.0636$ Ah for the LFP cell. Moreover, the discharge and charge ampere-hours at the start of the discharge and charge steps were not exactly zero, and therefore a subtraction of this value to the rest of the measured charge and discharge ampere-hours was performed to achieve a defined OCV curve at the endpoints of 0 % SOC and 100 % SOC.

The approximated OCV curve for both cells is the average of the discharge and charge OCV curves, with a minor modification. The modification is needed because, for both cells, the charge curve does not reach 100 % SOC before it reaches its cut-off voltage. This is due to the small ohmic polarization that is present during the tests [30]. Hence when averaging the two curves, there are no defined OCVs for the higher SOCs along the average OCV curve. For the NMC cell, the last points on the average OCV curve was found by simply creating a line of datapoints between the last available datapoint until the cut-off voltage at 100 % SOC. For the LFP cell, the average OCV curve was extrapolated manually by adding the OCV points from the discharge curve plus the difference between the last point on the average curve and the corresponding point on the discharge OCV curve. The resulting curves for both cells can be seen in Figure 5.4 and Figure 5.5. With the mentioned approximations and modifications, the conditions that the OCV-SOC curve shall not have any abrupt transitions nor be defined outside the cut-off voltage interval are satisfied [21].

Note that due to a difference in sampling time for the charge and discharge steps for the NMC cell, linear interpolation was used to make the datasets equal in length. Specifically the MATLAB function *interp1* was used.

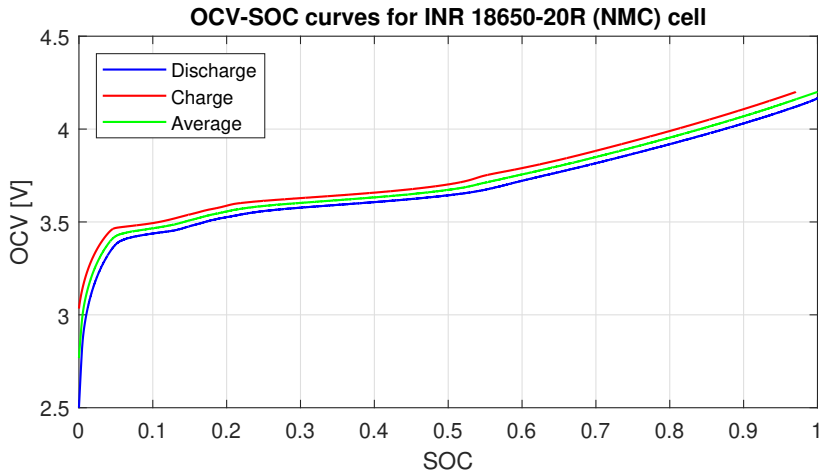

Figure 5.4: Final OCV-SOC curves for the INR 18650-20R (NMC) cell at an ambient temperature of 25 °C.

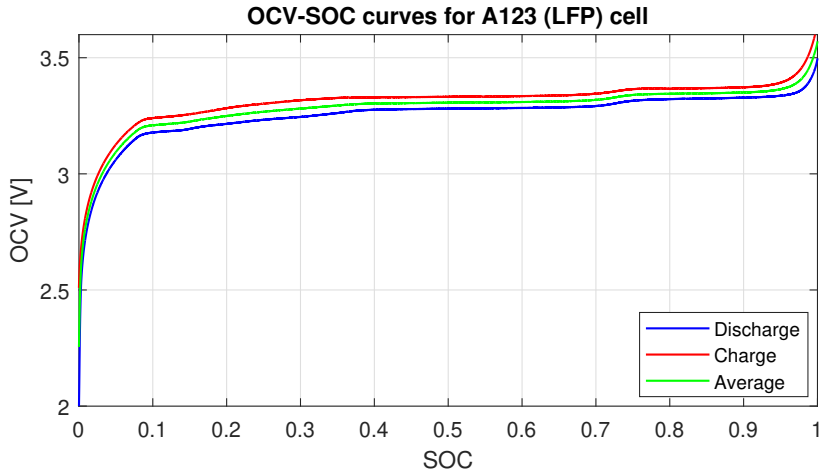

Figure 5.5: Final OCV-SOC curves for the A123 (LFP) cell at an ambient temperature of 25 °C.

5.2.2 OCV-SOC polynomial approximation

For the state estimation part of this thesis, the determined, average OCV-SOC relationship presented in the previous subsection was further approximated by a 12th-order polynomial. Here the MATLAB function *polyfit* was used to fit a polynomial function to the determined average OCV curve. The reason for this was mainly due to the structure of the MHE, which required the OCV curve to be expressed as a function rather than e.g. a lookup table, in order for the measurement equation to be included in the optimization problem. Moreover, it simplified the process of finding the (smoothed) derivative of the OCV-SOC curve, which is required in the EKF implementation. Often this derivative is found empirically and can therefore be noisy [21]. For this purpose the MATLAB function *polyder* was used with the OCV polynomial. The order of the polynomial approximation was chosen to be a high number to get a very accurate approximation, minimizing the propagation of error into the state estimation. Also, the order was chosen to be an even number to avoid the function crossing the upper cut-off voltage before 100 % SOC.

5.3 Parameter identification

For parameter identification of the models presented in Section 3.3, MATLAB code based on [16] was used. The script utilizes nonlinear regression and the DST load current as input to find the model parameters that make the model output fit the measured DST voltage. Specifically, the MATLAB function *nlinfit* and several cycles of the DST load current profile as input was used for identifying the R, RC1, and ESC model parameters of both cell types. For the NMC cell identification, 28 DST cycles were used, which corresponded to a change in SOC from 80% to 6%. For the LFP cell, 18 DST cycles were used, which corresponded to a change in SOC from 100% to 17%. Here it should be noted that the SOC range for which the model identification was performed was retracted somewhat, to

achieve reasonable model parameters. This was possibly due to the strong nonlinearities present at the end of the SOC range around 0 % SOC, which turned out to cause rank deficiencies that had a negative impact on the utilized regression method, which then again resulted in very poor and unrealistic parameter estimates. Note also that the battery data for the two cell types differ slightly, considering the LFP cell had available DST data for the entire SOC range, whereas the NMC cell only had available data for SOC $\leq 80\%$.

Early experimentation showed that the SOC range over which the model parameter identification was performed, had a significant impact on the estimated model parameters. What was equally important to note, was that due to the nonlinear nature of the models, reasonable initialization of the parameter values was also crucial [21]. This was especially true for the ESC model, which could achieve several different parameter values depending on the set initial value of the parameters and the set SOC range the parameters were estimated over. This was not put too much effort into, due to the wide scope of the thesis. Therefore the model identification was limited to the description above.

5.4 Observability analysis

Observability analysis of nonlinear battery ECMs has to some degree been researched in the literature, and to the extent that it will be adopted for the models used in this thesis. The 2RC model, which is similar to the 1RC model but only with a second RC sub-circuit, has been investigated previously in i.a. [37], where a slightly different choice of model states has been used. The analysis can be simplified and modified somewhat for the 1RC model used here, which is what will be presented in the following.

The continuous time 1RC model presented in Section 3.2 can be written on the form

$$\dot{\mathbf{x}} = \mathbf{f}(\mathbf{x}) + \mathbf{g}u \tag{5.1a}$$
$$y = h(\mathbf{x}) - R_0 u \tag{5.1b}$$

where $\mathbf{x} = [z, i_{R_1}]^T$, $u = i$, $y = v$ and

$$\mathbf{f}(\mathbf{x}) = \begin{bmatrix} 0 \\ -\frac{1}{R_1 C_1} i_{R_1} \end{bmatrix}, \quad \mathbf{g} = \begin{bmatrix} -\frac{1}{Q} \\ \frac{1}{R_1 C_1} \end{bmatrix}, \quad h(\mathbf{x}) = OCV(z) - R_1 i_{R_1}$$

Then, based on theory introduced in Section 2.4, the gradient of $\mathbf{h}(\mathbf{x})$ is

$$\mathbf{d}h = \begin{bmatrix} \frac{dOCV}{dz} & -R_1 \end{bmatrix}$$

and it can be shown by mathematical induction that

$$\mathbf{d}L_f^k h = \begin{bmatrix} 0 & -\frac{R_1}{(-R_1C_1)^k} \end{bmatrix}, \quad \mathbf{d}L_g^k h = \begin{bmatrix} \frac{1}{(-Q)^k}\frac{d^{k+1}OCV}{dz^{k+1}} & 0 \end{bmatrix}$$

Then the 1RC model is locally observable at a point $\mathbf{x}_0$ if the rank of the matrix

$$\mathcal{O} = \begin{bmatrix} \mathbf{d}h \\ \mathbf{d}L_f h \\ \mathbf{d}L_g h \\ \mathbf{d}L_f^2 h \\ \mathbf{d}L_g^2 h \\ \vdots \end{bmatrix} \tag{5.2}$$

evaluated at $\mathbf{x}_0$ has rank $n = 2$. It can be verified that this is the case if and only if there exists a positive integer $k \in \mathbb{Z}^+$ such that

$$\left(\frac{d^k OCV}{dz^k}\right)(\mathbf{x}_0) \neq 0 \tag{5.3}$$

meaning the 1RC model is observable at a point $\mathbf{x}_0$ if all derivatives of the OCV curve evaluated at that point are not zero simultaneously. This requirement will have to be satisfied for guaranteeing the observability of the R model as well.

Observability analysis of the ESC model is more laborious due to the increased complexity of the model. In [49] an observability analysis was carried out of the ESC model by examining the minimum singular values of the observability matrix. It was found that if the load current $i = 0$, then the observability matrix loses rank, resulting in an unobservable model. The same conclusion was presented in [50]. It is crucial to note that the result in [49] is based on an assumption of a monotonically increasing OCV-SOC curve. Thus the remarks on the partial derivatives of the OCV curve in the preceding paragraph may also be relevant for the ESC model, because the OCV-SOC curve is not necessarily monotonically increasing. Also it should be noted that the instantaneous hysteresis memory variable s_k was not included in the measurement equation in these analyses.

In general, it is not enough for the observability matrix to have full rank (i.e. be nonsingular) to guarantee accurate state estimation. This is because the model may contain weakly observable modes. A weakly observable mode occurs when the observability matrix is ill-conditioned, or equivalently, close to being singular [51]. In [50], the condition number of the observability matrix for the ESC model with a constant load current was checked. The conclusion was that the SOC estimation problem using the ESC model was well-posed since the condition number was not considered too high for a 3x3 matrix.

Based on the above, it is clear that the nonlinearity of the OCV curve is of great significance for the observability of a given ECM. If the OCV curve is very flat or linear, potential zero crossings of the derivative of the OCV curve may be present, which can render the model unobservable or weakly observable, resulting in poor state estimation results. It is interesting to note that if the OCV derivative becomes zero, then the EKF, which is based on a first-order linearization of the model, is, in fact, unobservable at these specific points [37]. Moreover, steady-state SOC estimation using the ESC model with zero load current may be more problematic compared to when the system is excited with a dynamic load current.

5.5 Estimator initialization analysis

In order to quantify and understand the significance of reasonable initialization of the given nonlinear estimators, a *full factorial experiment* was performed. Here the two varying factors were the initial SOC state error covariance, i.e. the first entry in the Kalman filter covariance matrix, and the initial SOC guess error. The initial state error covariance represents the uncertainty in the initial SOC guess. The corresponding performance metric was the SOC RMS estimation error. For this purpose, two sets of 11 initial values for the SOC and the SOC covariance were set to

$$\mathbf{z}_0 = \begin{bmatrix} 0 & 0.1 & 0.2 & 0.3 & 0.4 & 0.5 & 0.6 & 0.7 & 0.8 & 0.9 & 1 \end{bmatrix}$$

$$\sigma_{z,0} = \begin{bmatrix} 1 & 10^{-1} & 10^{-2} & 10^{-3} & 10^{-4} & 10^{-5} & 10^{-6} & 10^{-7} & 10^{-8} & 10^{-9} & 10^{-10} \end{bmatrix}$$

For evaluation of each combination from these two sets on the estimator performance, $11 \times 11 = 121$ simulations using the full FUDS cycles run for the NMC cellt was performed. Here the true initial SOC was 80 %, while the uncertainties of the current sensor (process noise) and the voltage sensor (measurement noise) was set to

$$\sigma_w = 0.1^2, \quad \sigma_v = 0.1^2$$

respectively. Finally, the initial covariance of the two remaining states in the utilized 1RC model was held constant at $\sigma_{i_{R,0}} = 0.01^2$, while the initial value of the state itself was set to 0 throughout the whole experiment.

5.6 State estimator implementation

5.6.1 EKF

The extended Kalman filter (EKF) was implemented in MATLAB based on code found in [30], which is a realization of algorithm 1. Here some changes to the code were made, so that the filter could be used with three different models. This essentially required the implementation of three similar EKFs. Since the ESC model contains all the states of the R and RC1 models, the derivation, also based on [30], of the EKF matrices is presented below only for the ESC model. In order to implement the EKF with the ESC model, some assumptions were made. First, the process noise was assumed to represent the current sensor measurement error, such that the true cell current was $i_k + w_k$. This implied that the measured cell current was i_k. This assumption was only used when deriving the linearized state matrices and not the linearized output matrices, to avoid creating a correlation between process noise and overall noise in the output measurement. Secondly, the couloumbic efficiency was assumed to be $\eta_k = 1$, which simplified the model. This was reasonable since the EKF's adaptive capability can handle any small error caused by this assumption. In the implementation of the EKF, the true cell current was i_k and the process noise was assumed to have zero mean, i.e. $\bar{w} = 0$. Thus, when the state vector was defined as $\mathbf{x}_k = [z_k, i_{R_1,k}, h_k]^T$, the final linearized and implemented state and output matrices became

$$\hat{\mathbf{A}}_k = \left.\frac{\partial \mathbf{f}(\mathbf{x}_k, \mathbf{u}_k, \mathbf{w}_k)}{\partial \mathbf{x}_k}\right|_{\mathbf{x}_k = \hat{\mathbf{x}}_k^+} = \begin{bmatrix} 1 & 0 & 0 \\ 0 & \exp(-\frac{\Delta t}{R_1 C_1}) & 0 \\ 0 & 0 & A_{H,k} \end{bmatrix} \tag{5.4}$$

where

$$A_{H,k} = \exp\left(-\left|\frac{i_k \gamma \Delta t}{Q}\right|\right)$$

$$\hat{\mathbf{B}}_k = \left.\frac{\partial \mathbf{f}(\mathbf{x}_k, \mathbf{u}_k, \mathbf{w}_k)}{\partial \mathbf{w}_k}\right|_{\mathbf{w}_k = \bar{\mathbf{w}}_k} = \begin{bmatrix} -\frac{\Delta t}{Q} \\ 1 - \exp(-\frac{\Delta t}{R_1 C_1}) \\ -\left|\frac{\gamma \Delta t}{Q}\right| A_{H,k}(1 + i_k \hat{h}_k^+) \end{bmatrix} \tag{5.5}$$

$$\hat{\mathbf{C}}_k = \left.\frac{\partial \mathbf{g}(\mathbf{x}_k, \mathbf{u}_k, \mathbf{v}_k)}{\partial \mathbf{x}_k}\right|_{\mathbf{x}_k = \hat{\mathbf{x}}_k^-} = \begin{bmatrix} \left.\frac{\partial OCV(z_k)}{\partial z_k}\right|_{z_k = \hat{z}_k^-} & -R_1 & M \end{bmatrix} \tag{5.6}$$

where $\left.\frac{\partial OCV(z_k)}{\partial z_k}\right|_{z_k = \hat{z}_k^-}$ is the partial derivative of the OCV polynomial approximation evaluated at the a priori SOC estimate $\hat{z}_k^-$.

$$\hat{\mathbf{D}}_k = \left.\frac{\partial \mathbf{g}(\mathbf{x}_k, \mathbf{u}_k, \mathbf{v}_k)}{\partial \mathbf{v}_k}\right|_{\mathbf{v}_k = \bar{\mathbf{v}}_k} = 1 \tag{5.7}$$

Then the final tuning of the EKF resulted in the following covariance matrices:

$$\begin{gathered} \boldsymbol{\Sigma}_{\tilde{\mathbf{w}}} = 0.1^2, \quad \boldsymbol{\Sigma}_{\tilde{\mathbf{v}}} = 0.1^2. \\ \boldsymbol{\Sigma}_{\tilde{\mathbf{x}},0} = \begin{bmatrix} 0.1^2 & 0 & 0 \\ 0 & 0.01^2 & 0 \\ 0 & 0 & 0.01^2 \end{bmatrix} \end{gathered} \tag{5.8}$$

5.6.2 SPKF

The version of the Sigma-Point Kalman filter that was chosen for implementation in this thesis was the Central Difference Kalman filter (CDKF). The main reason for this was that it had fewer tuning parameters than the UKF, which made for a simpler implementation. The code is based on the MATLAB code found in [30], which is a realization of algorithm 2. Also here three different versions of the CDKF were implemented, in order to evaluate the CDKF performance using three different ECMs. The tuning parameter h was set to $\sqrt{3}$ since the noise is assumed to be Gaussian [30]. All tuning parameters were set to

γ	$\alpha_0^{(m)}$	$\alpha_k^{(m)}$	$\alpha_0^{(c)}$	$\alpha_k^{(c)}$
$\sqrt{3}$	$-\frac{2}{3}$	$\frac{1}{6}$	$-\frac{2}{3}$	$\frac{1}{6}$

Table 5.2: Tuning parameters of the CDKF.

$$\begin{gathered} \boldsymbol{\Sigma}_{\tilde{\mathbf{w}}} = 0.1^2, \quad \boldsymbol{\Sigma}_{\tilde{\mathbf{v}}} = 0.1^2. \\ \boldsymbol{\Sigma}_{\tilde{\mathbf{x}},0} = \begin{bmatrix} 0.1^2 & 0 & 0 \\ 0 & 0.01^2 & 0 \\ 0 & 0 & 0.01^2 \end{bmatrix} \end{gathered} \tag{5.9}$$

5.6.3 MHE

The MHE was implemented with inspiration from MATLAB code produced by Dr. Mohamed W. Mehrez, available on GitHub at [52] and demonstrated through video at [53]. His code is a combined implementation of a Model Predictive Controller (MPC) and a Moving Horizon Estimator (MHE) for a non-holonomic mobile robot, using the CasADi optimization toolbox in MATLAB. When setting up the nonlinear program (NLP) to be optimized, he utilizes multiple shooting. The MHE implemented in this thesis took advantage of the same techniques when adopting the nonlinear ECMs for the NMC and LFP

cells for SOC estimation. The reason for using multiple shooting was mostly based on the fact that early experimentation showed that this approach could achieve more accurate state estimations when compared to using single shooting, which was to be anticipated for reasons stated in Section 2.3.3. Hence the optimization variables of the nonlinear program became the system states $\mathbf{x}$ as well as the control input $\mathbf{u}$ for all models and cells. The implementation is also based on the *total least squares* MHE (TLS-MHE) as formulated in [13], which essentially co-estimates the state and input of the model. Thus the MHE formulation opted for in this thesis was set up as

$$\begin{aligned}
\min_{\hat{\mathbf{x}},\hat{\mathbf{u}}} \ & \|\hat{\mathbf{x}}_{k-N+1} - \bar{\mathbf{x}}_{k-N+1}\|^2_{P^{-1}_{k-N+1}} + \sum_{i=k-N+1}^{k} \|y_i - h(\hat{\mathbf{x}}_i, \hat{u}_i)\|^2_{R^{-1}} \\
& + \sum_{i=k-N+1}^{k} \|u_i - \hat{u}_i\|^2_{Q^{-1}} \\
& s.t. \\
& \bar{\mathbf{x}}_{k-N+1} \quad \text{given} \\
& y_{k-N+i} \quad \text{given}; \quad i = 1, ..., N \\
& u_{k-N+i} \quad \text{given}; \quad i = 1, ..., N \\
& \hat{\mathbf{x}}_{k-N+i+1} = \mathbf{f}(\hat{\mathbf{x}}_{k-N+i}, \hat{u}_{k-N+i}); \quad i = 1, ..., N \\
& 0 < \hat{z}_k < 1
\end{aligned} \tag{5.10}$$

where $\mathbf{f}(\hat{\mathbf{x}}_{k-N+i}, \hat{u}_{k-N+i})$ is the dynamic state equations evaluated in the state and input estimates, and $h(\hat{\mathbf{x}}_i, \hat{u}_i)$ is the output equation for the relevant model also evaluated in the estimates. The arrival cost penalization matrix was approximated by running the EKF state error covariance updates from Section 5.6.1 in parallel with the MHE. One subtlety is that the MHE for each time step k also computed the predicted state for time step $k+1$. This prediction was stored and used as the a priori state estimate $\bar{\mathbf{x}}_{k-N+1}$ in the arrival cost next time step [54]. This ensured that all information from measurements prior to the current estimation horizon was contained in the arrival cost, thus avoiding using any given measurement twice. The NLP solver that was used was the IPOPT solver, which was part of the CasADi toolbox. The operation of the MHE algorithm in this thesis can be summarized as

1. Initialize $\mathbf{Q}$, $\mathbf{R}$, $\mathbf{P}$, N and $\hat{\mathbf{x}}_0$
2. If $k \leq N$ solve the full information estimation problem, i.e. with increasing horizon length for each iteration until $k = N$. Obtain the optimal solutions $\{\hat{\mathbf{x}}_i\}^k_{i=k-N+1}$ and load current estimates $\{\hat{u}_i\}^k_{i=k-N+1}$. Store these as initial conditions for the next iteration.
3. If $k > N$ solve the NLP in (5.10) and obtain the optimal solutions $\{\hat{\mathbf{x}}_i\}^k_{i=k-N+1}$ and load current estimates $\{\hat{u}_i\}^k_{i=k-N+1}$. Store these as initial conditions for the next iteration.

4. At time $k+1$ get the new measurements y_{k+1} and u_{k+1} and discard the first measurements in the horizon from time step k, then return to step 3 again.

The final tuning parameters of the MHE were set to

$$\mathbf{Q} = 0.1^2, \quad \mathbf{R} = 0.1^2, \quad N = 10$$

$$\mathbf{\Sigma}_{\tilde{\mathbf{x}},0} = \begin{bmatrix} 0.1^2 & 0 & 0 \\ 0 & 0.01^2 & 0 \\ 0 & 0 & 0.01^2 \end{bmatrix} \tag{5.11}$$

5.6.4 Tuning

The tuning process of the estimators involved choosing the constant weighting matrices $\mathbf{\Sigma}_{\tilde{\mathbf{w}}}$ and $\mathbf{\Sigma}_{\tilde{\mathbf{v}}}$ for the Kalman filters, and $\mathbf{Q}$ and $\mathbf{R}$ for the MHE, which was defined to represent the uncertainties in the current and voltage measurements respectively. The tuning also included setting the initial state error covariance matrix $\mathbf{\Sigma}_{\tilde{\mathbf{x}},0}$ for all the estimators, as well as choosing a horizon length N for the MHE and the tuning parameter h for the SPKF. The strategy for setting the covariance matrices was to use an initial guess based on the measurement uncertainties for the Arbin BT2000 battery test bench, from which the battery test data was collected, which is below 0.1% for both the current and voltage sensors [55]. Hence a standard deviation of 0.001 and consequently a covariance of 0.001^2 was set initially for all covariance matrices. Afterward, the strategy was simply based on trial and error to achieve a reasonably good tuning. The initial SOC state error covariance was set to the square of the difference between the initial guess SOC and the true initial SOC, where the true SOC has been defined by the dataset to be 0.8. Hence the initial SOC covariance represents confidence in the initial guess SOC. Note that it is not possible to know this difference exactly in a real-time BMS application, only in simulations where a ground truth has been established in order to perform a performance evaluation of the estimators. When using the RC1 or ESC model, the covariances of the RC-sub-circuit current and hysteresis states were set quite low because one with high confidence can say that these are close to zero initially assuming the cell has been resting for a while. For a fair comparison of the estimators, a similar tuning for all estimators regardless of model and cell type was chosen. Therefore the tuning parameters are presented only for the ESC model. The tuning also holds for the lower-order models. Here the redundant entries in the matrices were simply omitted, whereas the relevant entries remained unchanged.

When choosing the horizon length N for the MHE, the FUDS cycles with additive random noise (see Section 5.7.3) and the NMC-ESC model were used for experimentation. Different horizon lengths were evaluated against the corresponding RMS SOC estimation error and the average required computation time per iteration, to find an appropriate horizon length that yielded a low estimation error at a reasonable computational cost. This horizon length was held fixed for all models, cells, and inputs. The experiment is summarized in Table 5.3. For fair comparison and a reasonable balance between estimation performance and computational cost, a horizon length of $N = 10$ was chosen.

N	RMSE	Avg. computation time per iteration
2	2.42 %	0.0174 s
5	2.29 %	0.0281 s
10	2.17 %	0.0444 s
20	2.02 %	0.0779 s
50	1.78 %	0.178 s
100	1.57 %	0.348 s
200	1.39 %	0.682 s

Table 5.3: Summary of sub-experiment for finding a reasonable MHE horizon length N.

5.7 Simulation setup

For the performance evaluation of the state estimators with the different models and cell chemistries, three different simulation cases were set up. All simulations were run in MATLAB on the NTNU master office computer with 11th gen. Intel Core i7-11700 @ 2.50 GHz, 32 GB RAM, and Windows operating system. For all subsequent dynamic simulations, the initial SOC of the estimators was set erroneously to 0.7, which corresponded to an initial SOC estimation error of 10 %.

5.7.1 Ground truth

Although it is impossible to define the absolute true SOC of a battery, it can be established accurately with the coulomb counting method under controlled conditions. Since the current data from the dataset have been collected by lab-grade equipment (the Arbin BT2000 battery test bench) at a constant temperature [45, 46], it is assumed that the current is measured perfectly. The ground truth has therefore been established by integrating the relevant current data with the MATLAB function *cumtrapz*. The accumulated charge in and out of the battery divided by the nominal capacity at a given timestep subtracted to the true initial SOC of 0.8, resulted in the SOC ground truth. The estimation performance of the estimators was quantified by taking the root mean square error (RMSE) and the mean absolute error (MAE) between the ground truth and the SOC estimates.

5.7.2 Simulation 1 - Dynamic load profiles

The first simulation case was purely based on using the dynamic load profiles from FUDS and US06 directly as input for all estimator/model/cell combinations and comparing the estimation accuracy. The full current and voltage measurement data for the FUDS run is shown for the NMC cell in Figure 5.6, whereas the full US06 input is shown for the LFP cell in Figure 5.7.

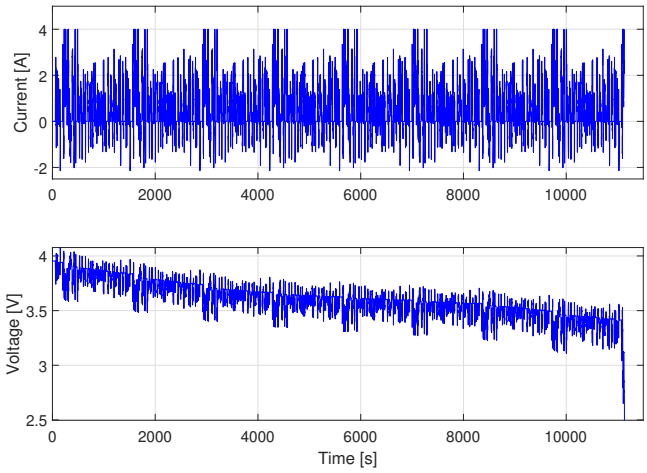

Figure 5.6: The full FUDS load profile for the NMC cell at 25 °C.

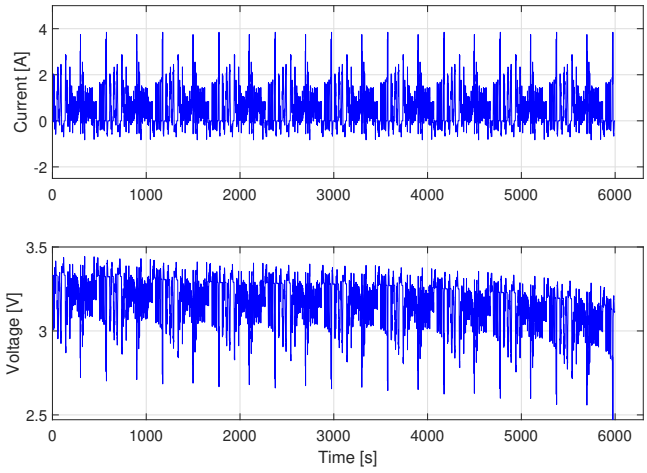

Figure 5.7: The full US06 load profile for the LFP cell at 25 °C.

5.7.3 Simulation 2 - Dynamic load profiles with added measurement noise

In the second simulation case, heavy simulated EMI noise was added to the measurements, to investigate the performance under non-ideal working conditions, as can often be the case in real-world EV applications. Here only the FUDS cycles were used, with added random noise to both current and voltage measurements. Most commercial current and voltage

sensors in Battery Management Systems have a measurement error of 0.1 % to 1 % [56] of the measurement range. Based on this, random current and voltage sensor noise with a standard deviation of 240 mA and 80 mV respectively were added to the input data, to simulate noisy measurements. These values correspond to approximately 4 % of the relevant measurement range. It should be mentioned that any larger values seemed to cause unacceptable estimation performance.

5.7.4 Simulation 3 - Dynamic load profiles with resting periods

The third simulation was set up to investigate the steady-state estimation performance of the estimators, by adding resting periods to the dynamic load profiles. This was implemented by adding steady-state input data to the start, middle, and end of the dynamic load profile runs. The length of these periods was set to 1 hour. During a resting period, zero load current was applied to the models, and the newest reasonable steady-state voltage measurement was held constant. Here only the FUDS cycles were used as the dynamic profile.

6

Results

This section documents the results from the the methodology of this thesis presented in Chapter 5. Here the results of the OCV-SOC polynomial approximations are presented in Section 6.1, the results of the model identifications in Section 6.2, the estimator initialization results in Section 6.3 and the final dynamic simulation results in Section 6.4.

6.1 OCV-SOC polynomial approximation

In Figure 6.1 and Figure 6.2 the 12th-order polynomial OCV curve fitted to the approximated average OCV curve for each cell can be observed. In Table 6.1 the coefficients of the polynomial for each cell are listed. Thus the OCV-SOC curve, as seen by the estimators, is represented by the function

$$OCV(z) = \sum_{i=0}^{n} a_i z^i, \quad z \in [0, 1] \tag{6.1}$$

where n is the polynomial order. The resulting partial derivative of each OCV polynomial, $\frac{\partial OCV(z)}{\partial z}$, can be seen in Figure 6.3 and Figure 6.4.

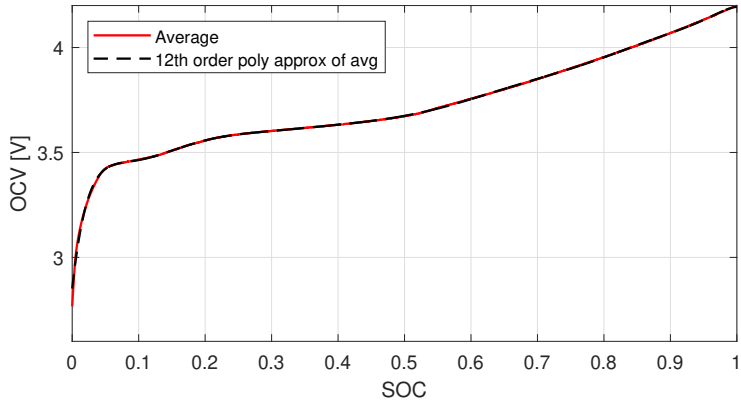

Figure 6.1: Polynomial approximation of the average OCV-SOC curve for the INR 18650-20R (NMC) cell at an ambient temperature of 25 °C.

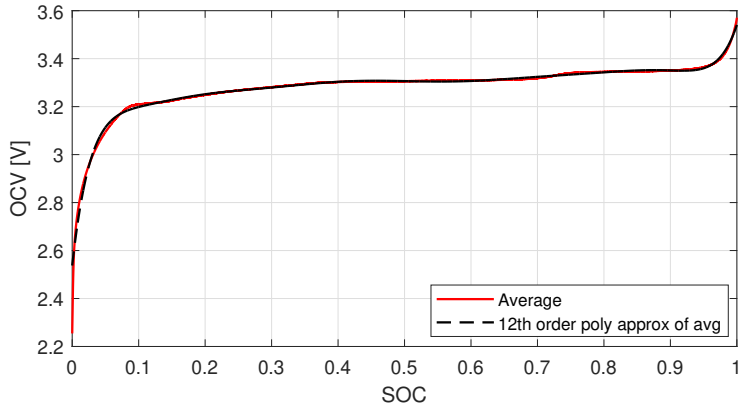

Figure 6.2: Polynomial approximation of the average OCV-SOC curve for the A123 (LFP) cell at an ambient temperature of 25 °C.

	NMC	LFP
a_0	2.8518	2.5375
a_1	28.5684	24.7599
a_2	-575.5558	-417.4004
a_3	6.3657e3	4.0803e3
a_4	-4.2526e4	-2.5009e4
a_5	1.8416e5	1.0106e5
a_6	-5.3862e5	-2.7705e5
a_7	1.0848e6	5.2184e5
a_8	-1.5061e6	-6.7378e5
a_9	1.4155e6	5.8439e5
a_{10}	-8.5947e5	-3.2440e5
a_{11}	3.0415e5	1.0373e5
a_{12}	-4.7628e4	-41

Table 6.1: The identified coefficients of the 12th-order OCV-SOC polynomial approximation of each cell at an ambient temperature of 25°C.

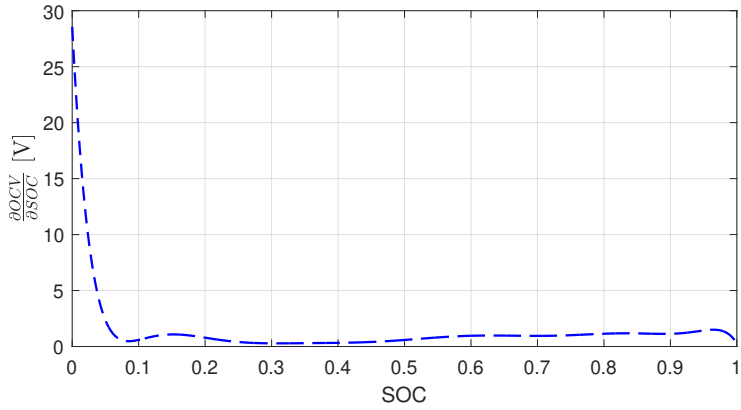

Figure 6.3: Partial derivative of polynomial OCV-SOC curve for the INR 18650-20R (NMC) cell at an ambient temperature of 25 °C.

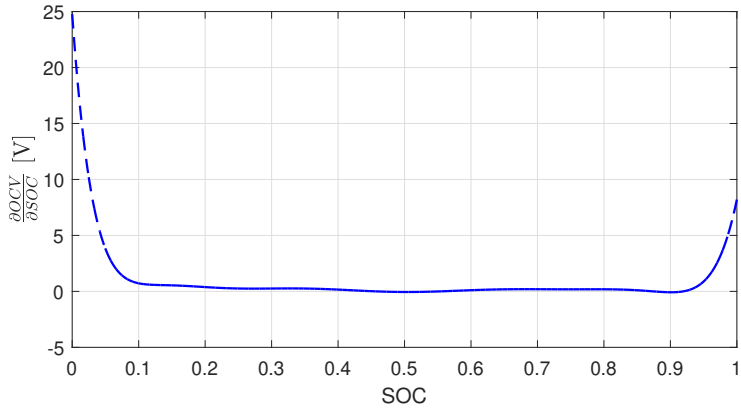

Figure 6.4: Partial derivative of polynomial OCV-SOC curve for the A123 (LFP) cell at an ambient temperature of 25 °C.

6.2 Identified models

This section summarizes the results from the model identification of each cell using non-linear regression. The identified models output can be seen in Figure 6.5 for the NMC-R model, and in Figure 6.6 and Figure 6.7 for the LFP-RC1 and LFP-ESC models, respectively. All parameters for each cell type and model combination can be seen in Table 6.2, along with the corresponding RMS model fit error.

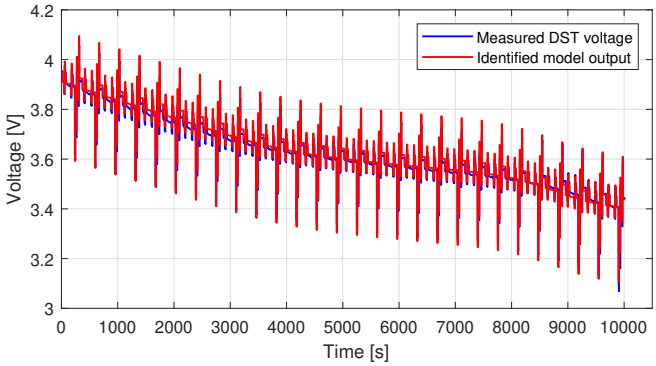

Figure 6.5: Identified R model output for the INR 18650-20R (NMC) cell at an ambient temperature of 25 °C.

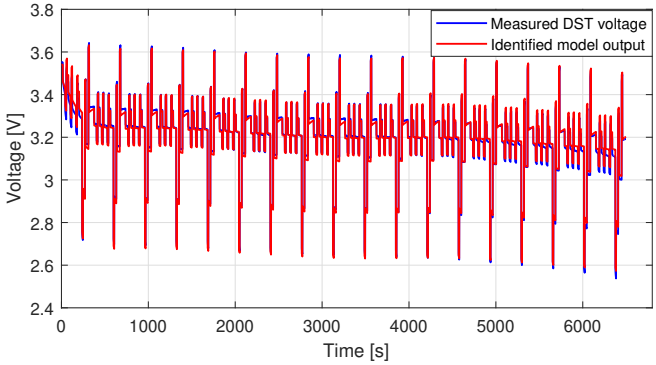

Figure 6.6: Identified RC1 model output for the A123 (LFP) cell at an ambient temperature of 25 °C.

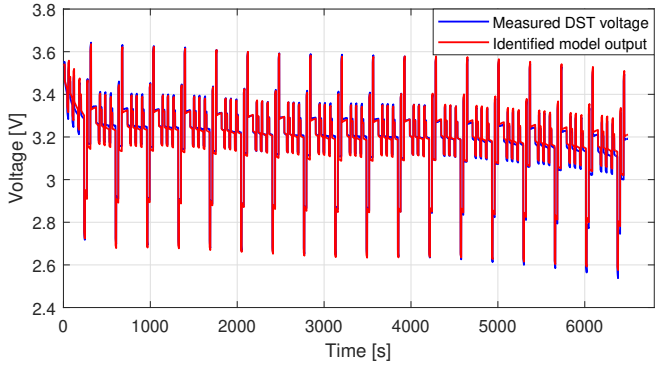

Figure 6.7: Identified ESC model output for the A123 (LFP) cell at an ambient temperature of 25 °C.

	$R_0(\Omega)$	$R_1(\Omega)$	$C_1(F)$	$M(V)$	$M_0(V)$	γ	RMSE
NMC-R	0.0855	-	-	-	-	-	0.0182
NMC-RC1	0.0758	0.0302	2037.0	-	-	-	0.0102
NMC-ESC	0.0732	0.0171	1467.2	0.0131	1.7796e-6	54.86	0.0098
LFP-R	0.1825	-	-	-	-	-	0.0365
LFP-RC1	0.1634	0.0749	1767.2	-	-	-	0.0142
LFP-ESC	0.1595	0.0365	2590.3	0.0381	9.3765e-4	93.63	0.0122

Table 6.2: Identified R, RC1 and ESC model parameters for NMC and LFP cell at an ambient temperature of 25 °C.

6.3 Estimator initialization

Below the results of the full factorial experiment on the SOC initialization of the estimators are presented. In each figure the SOC RMS estimation error after a full run of FUDS cycles using the NMC-1RC model is given along the z-axis. Along the right-hand side horizontal axis represents the initial SOC guess, and the left-hand side horizontal axis represents the initial SOC covariance in the Kalman filter covariance matrix. Recall that the true SOC is defined as 0.8.

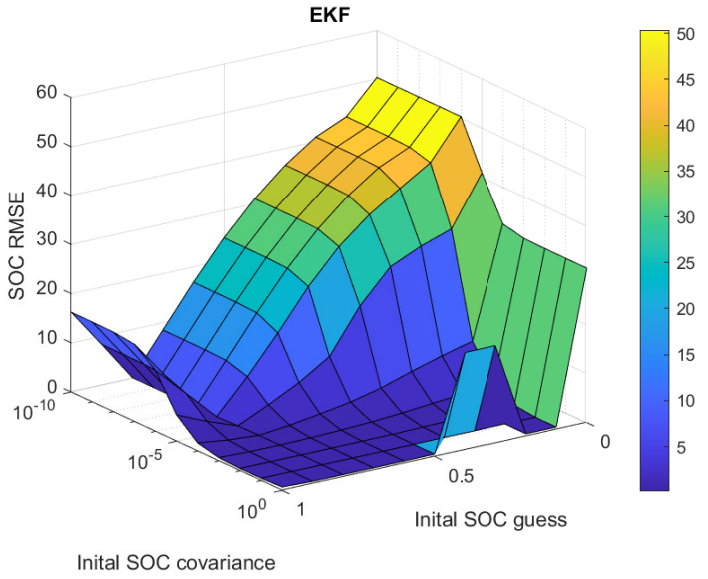

Figure 6.8: Surface plot of the full factorial experiment of the EKF initialization using a full run of FUDS cycles and the NMC-1RC model.

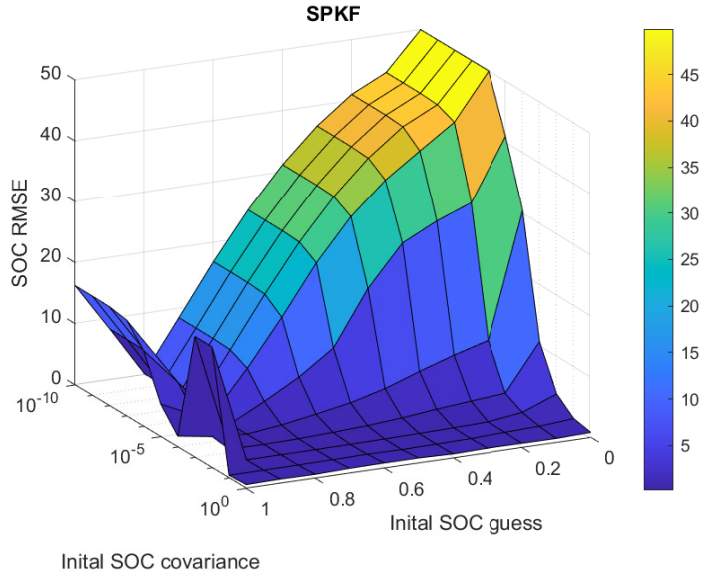

Figure 6.9: Surface plot of the full factorial experiment of the SPKF initialization using a full run of FUDS cycles and the NMC-1RC model.

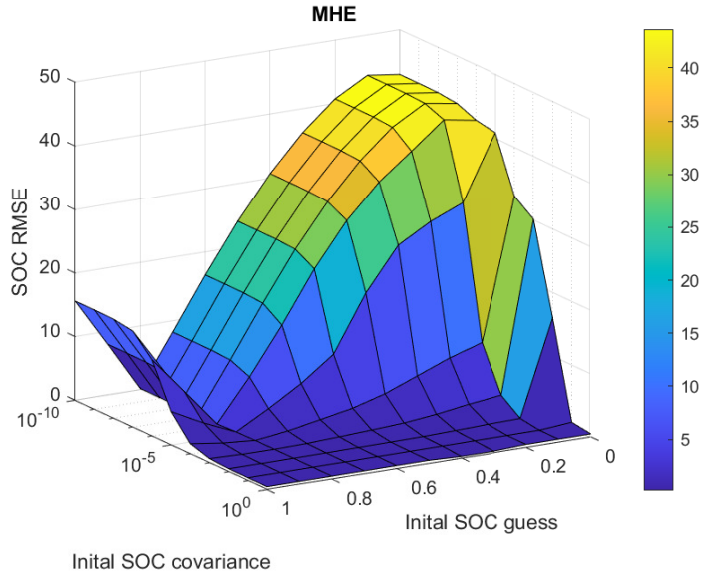

Figure 6.10: Surface plot of the full factorial experiment of the MHE initialization using a full run of FUDS cycles and the NMC-1RC model.

6.4 Nonlinear state estimator performance

For each simulation case below, comparison plots that include a best-performing estimator-model combination for each cell type are given. Comparison plots that include one of the worst-performing combinations are also presented. The remaining results are summarized in tables. The relevant results are SOC estimation accuracy, MHE load current estimation accuracy, and estimator voltage output estimation accuracy. In the first simulation case, a comparison of the running times of the different estimators is presented, to evaluate their relative computational complexity.

6.4.1 Simulation 1 - Dynamic load profiles

FUDS

In Figure 6.11, the SOC estimates from all the nonlinear estimators are plotted using the NMC-ESC model with FUDS cycles as input. In this plot, a zoomed-in window has been included to highlight the difference in the estimates and the ground truth. The corresponding voltage estimates can be observed in Figure 6.12. The MHE load current estimates are found in Figure 6.13. All SOC results using the FUDS cycles are summarized in table Table 6.3, the output estimation results in Table 6.4 and MHE load current estimates in Table 6.5. In this subsection only, the average required computation time per iteration for the nonlinear estimators is presented in Table 6.6. For the discussion of the results, see Section 7.1.

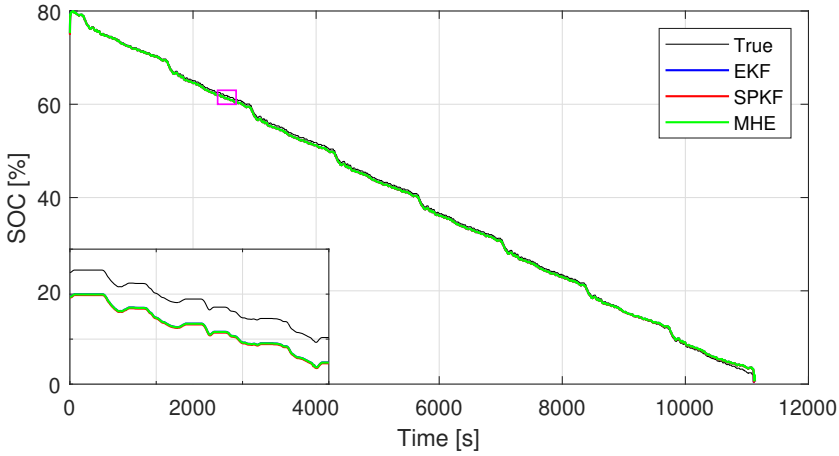

Figure 6.11: SOC estimation comparison using the NMC-ESC model during FUDS cycles at an ambient temperature of 25 °C. An additional zoomed-in plot of the highlighted box period is added in the bottom left corner.

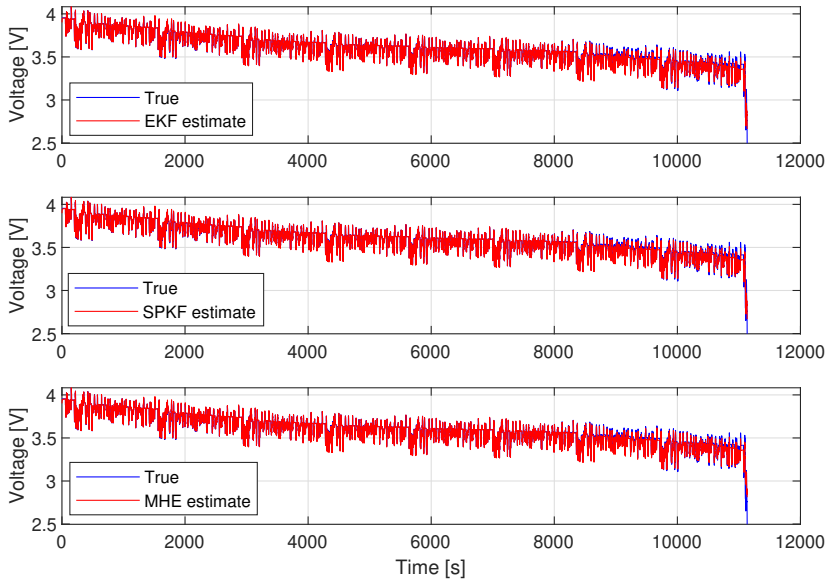

Figure 6.12: Output voltage estimation comparison using the NMC-ESC model during FUDS cycles at an ambient temperature of 25 °C.

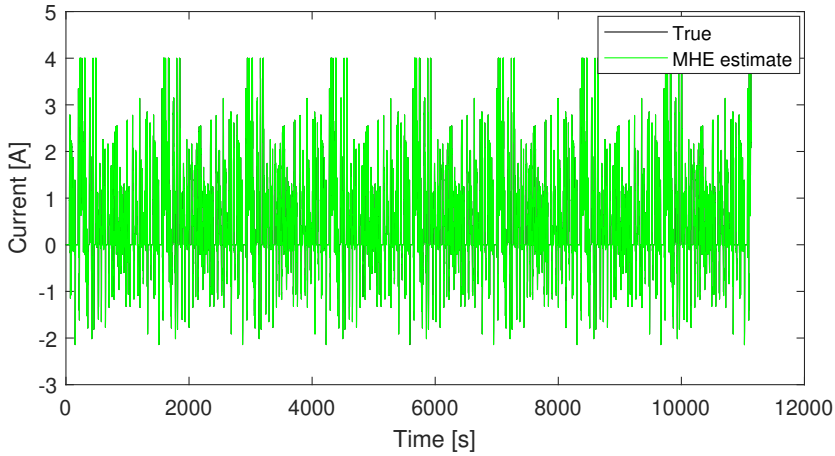

Figure 6.13: MHE load current estimation using the NMC-ESC model during FUDS cycles at an ambient temperature of 25 °C.

	EKF		SPKF		MHE	
	RMSE	MAE	RMSE	MAE	RMSE	MAE
NMC-R	1.50 %	1.44 %	1.51 %	1.44 %	1.51 %	1.44 %
NMC-RC1	0.46 %	0.42 %	0.47 %	0.42 %	0.47 %	0.42 %
NMC-ESC	0.45 %	0.41 %	0.46 %	0.42 %	0.45 %	0.41 %
LFP-R	10.37 %	10.05 %	10.74 %	10.38 %	10.39 %	10.06 %
LFP-RC1	3.38 %	2.97 %	3.52 %	3.09 %	3.32 %	2.91 %
LFP-ESC	4.90 %	4.41 %	4.79 %	4.30 %	4.76 %	4.28 %

Table 6.3: Summary of SOC estimation RMSE and MAE for the estimators using different model and cell chemistry combinations with FUDS cycles as input.

	EKF		SPKF		MHE	
	RMSE	MAE	RMSE	MAE	RMSE	MAE
NMC-R	2.17 %	1.44 %	2.17 %	1.44 %	2.15 %	1.42 %
NMC-RC1	1.64 %	0.82 %	1.64 %	0.82 %	1.62 %	0.81 %
NMC-ESC	1.34 %	0.72 %	1.34 %	0.72 %	1.51 %	0.73 %
LFP-R	4.00 %	2.74 %	4.05 %	2.76 %	3.96 %	2.65 %
LFP-RC1	2.01 %	1.13 %	2.01 %	1.14 %	1.95 %	1.09 %
LFP-ESC	1.62 %	1.10 %	1.58 %	1.07 %	1.99 %	1.10 %

Table 6.4: Summary of output voltage estimation RMSE and MAE for the estimators using different model and cell chemistry combinations with FUDS cycles as input.

MHE load current estimate ($\hat{u}$)		
	RMSE	MAE
NMC-R	0.18 %	0.12 %
NMC-RC1	0.12 %	0.061 %
NMC-ESC	0.11 %	0.053 %
LFP-R	0.68 %	0.48 %
LFP-RC1	0.32 %	0.18 %
LFP-ESC	0.31 %	0.18 %

Table 6.5: Summary of the MHE load current estimation RMSE and MAE with the FUDS cycles.

Average computation time per iteration			
	EKF	SPKF	MHE
NMC-R	8.38e-6 s	2.76e-5 s	0.0411 s
NMC-RC1	1.21e-5 s	3.75e-5 s	0.0416 s
NMC-ESC	1.56e-5 s	4.25e-5 s	0.0456 s
LFP-R	9.77e-6 s	3.06e-5 s	0.0406 s
LFP-RC1	1.26e-5 s	3.45e-5 s	0.0412 s
LFP-ESC	1.66e-5 s	4.71e-5 s	0.0441 s

Table 6.6: Summary of average computation time required per iteration for the different estimator and model/cell type combinations during simulations with FUDS cycles.

US06

In Figure 6.15, the SOC estimates obtained from all the nonlinear estimators are plotted using the LFP-ESC model with US06 cycles as input. This was picked as the worst-performing cell-model combination in this case. The corresponding voltage estimates can be observed in Figure 6.16. The load current estimates obtained from the moving horizon estimator (MHE) are shown in Figure 6.17. All the SOC results using the US06 cycles are summarized in Table 6.7, the output estimation results are provided in Table 6.8, and the MHE load current estimates in Table 6.9. An additional SOC estimates comparison of the best-performing model-cell combination for the LFP cell is observed in Figure 6.14. For the discussion of the results, see Section 7.1.

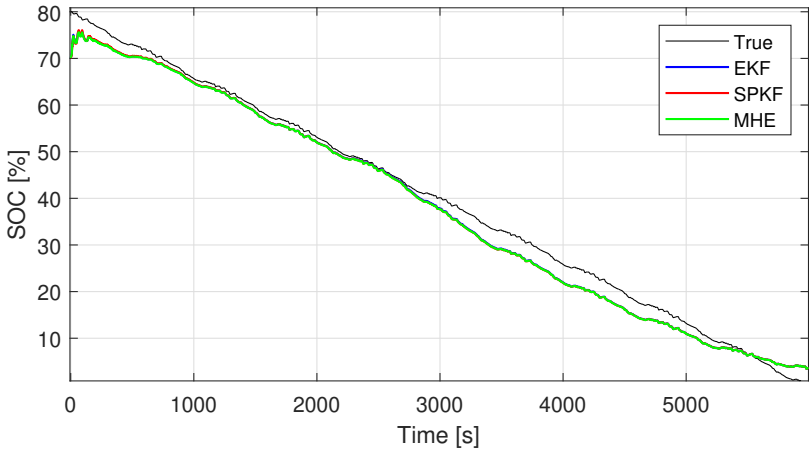

Figure 6.14: SOC estimation comparison using the LFP-R model during US06 cycles at an ambient temperature of 25 °C.

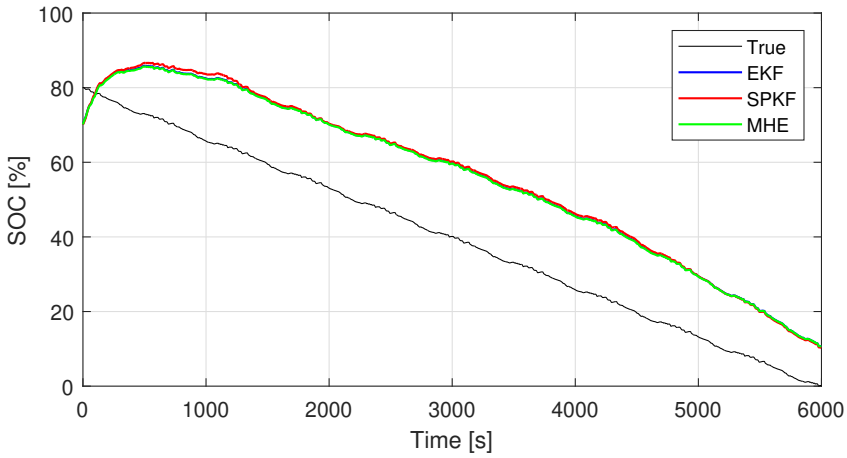

Figure 6.15: SOC estimation comparison using the LFP-ESC model during US06 cycles at an ambient temperature of 25 °C.

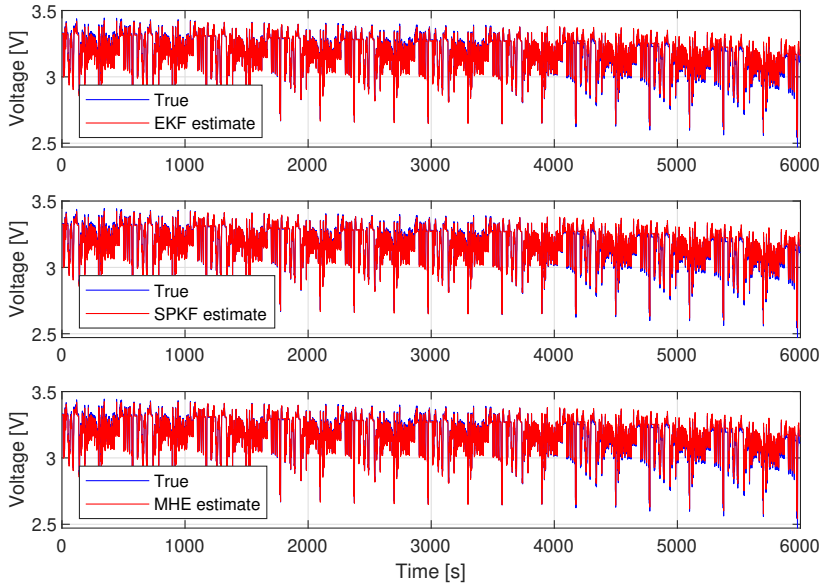

Figure 6.16: Output voltage estimation comparison using the LFP-ESC model during FUDS cycles at an ambient temperature of 25 °C.

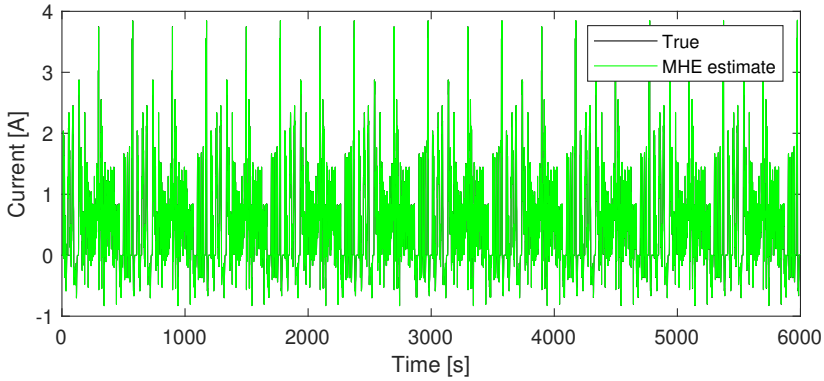

Figure 6.17: MHE load current estimation using the LFP-ESC model during FUDS cycles at an ambient temperature of 25 °C.

	EKF		SPKF		MHE	
	RMSE	MAE	RMSE	MAE	RMSE	MAE
NMC-R	1.35 %	1.32 %	1.35 %	1.33 %	1.36 %	1.33 %
NMC-RC1	0.43 %	0.31 %	0.44 %	0.31 %	0.44 %	0.31 %
NMC-ESC	0.46 %	0.25 %	0.45 %	0.26 %	0.46 %	0.26 %
LFP-R	2.49 %	2.11 %	2.53 %	2.15 %	2.55 %	2.19 %
LFP-RC1	11.82 %	11.49 %	12.10 %	11.77 %	11.69 %	11.38 %
LFP-ESC	16.86 %	16.45 %	17.28 %	16.84 %	16.75 %	16.34 %

Table 6.7: Summary of SOC estimation RMSE and MAE for the estimators using different model and cell chemistry combinations with US06 cycles as input.

	EKF		SPKF		MHE	
	RMSE	MAE	RMSE	MAE	RMSE	MAE
NMC-R	1.03 %	0.82 %	1.03 %	0.82 %	1.02 %	0.81 %
NMC-RC1	1.49 %	0.81 %	1.49 %	0.67 %	1.48 %	0.80 %
NMC-ESC	1.43 %	0.78 %	1.45 %	0.79 %	1.42 %	0.78 %
LFP-R	2.81 %	2.06 %	2.81 %	2.06 %	2.74 %	2.00 %
LFP-RC1	1.20 %	1.00 %	1.20 %	1.00 %	1.16 %	0.97 %
LFP-ESC	1.67 %	1.37 %	1.63 %	1.34 %	1.62 %	1.33 %

Table 6.8: Summary of output voltage estimation RMSE and MAE for the estimators using different model and cell chemistry combinations with US06 cycles as input.

MHE load current estimate ($\hat{u}$)		
	RMSE	MAE
NMC-R	0.090 %	0.069 %
NMC-RC1	0.11 %	0.060 %
NMC-ESC	0.10 %	0.057 %
LFP-R	0.50 %	0.37 %
LFP-RC1	0.20 %	0.16 %
LFP-ESC	0.26 %	0.21 %

Table 6.9: Summary of the MHE load current estimation RMSE and MAE with the US06 cycles.

6.4.2 Simulation 2 - Dynamic load with noisy measurements

Figure 6.18 compares the SOC estimates obtained from all using the NMC-1RC model with noise-corrupted FUDS measurements as input. This particular combination represents a best-performing scenario in this simulation case. The corresponding voltage estimates can be observed in Figure 6.19. The load current estimates obtained from the moving horizon estimator (MHE) are shown in Figure 6.20. A plot of the best-performing LFP model for SOC estimation is included in Figure 6.21. Also, plots of the worst-performing combination, obtained using the LFP-ESC model, are provided in the Figure 6.22, Figure 6.23 and Figure 6.24. The plots are in the same order as the previous plots. As in the preceding subsections, all results are summarized in Table 6.10, Table 6.11, and Table 6.12. For the discussion of the results, see Section 7.1.

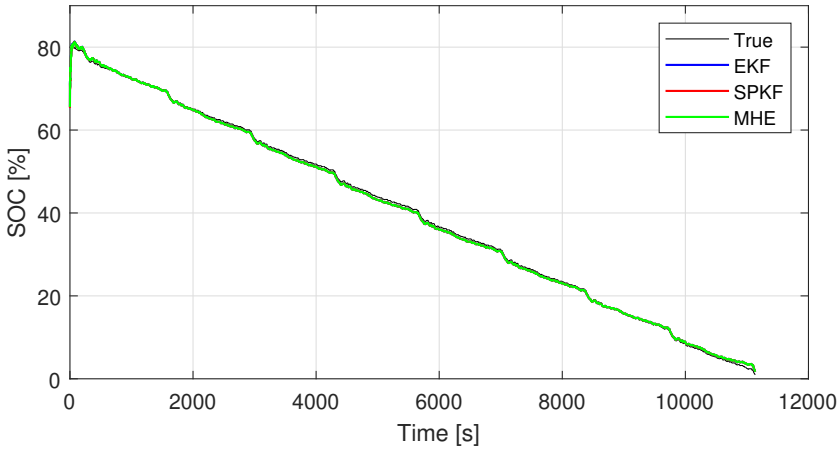

Figure 6.18: SOC estimation comparison using the NMC-1RC model during FUDS cycles with noisy measurements at an ambient temperature of 25 °C.

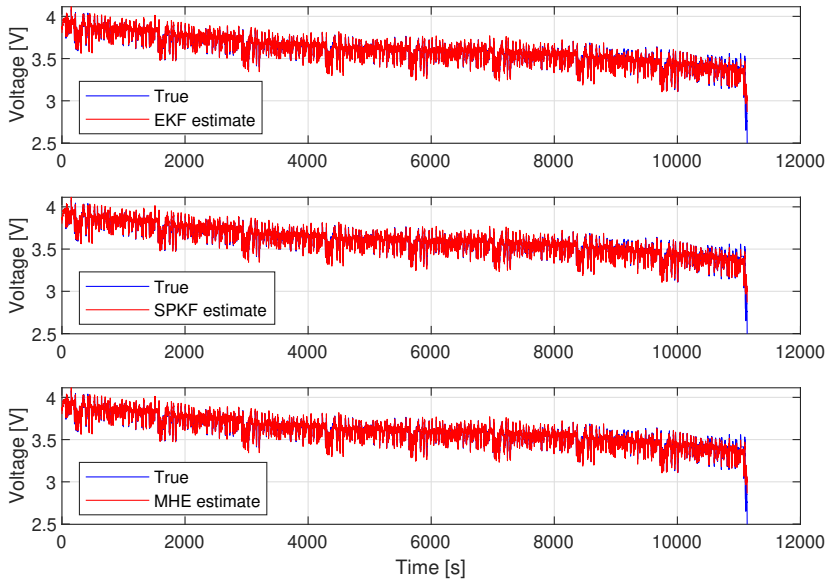

Figure 6.19: Output voltage estimation comparison using the NMC-1RC model during FUDS cycles with noisy measurements at an ambient temperature of 25 °C.

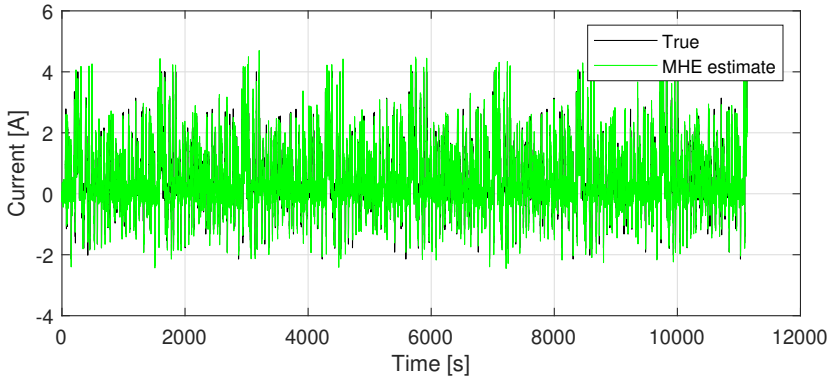

Figure 6.20: MHE load current estimation using the NMC-1RC model during FUDS cycles with noisy measurements at an ambient temperature of 25 °C.

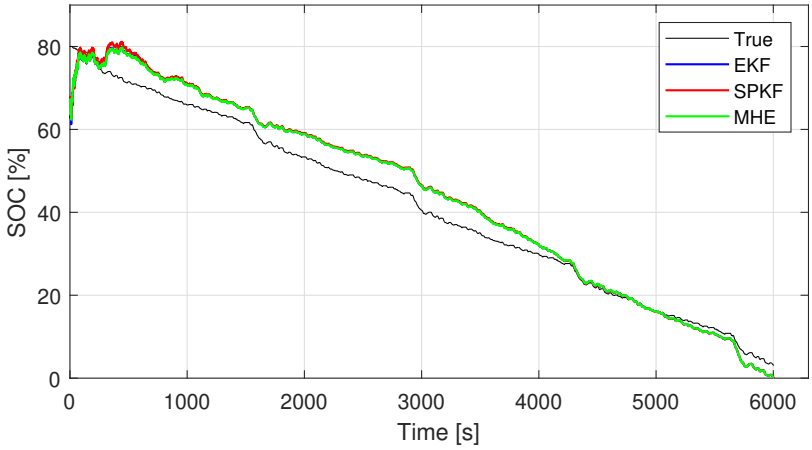

Figure 6.21: SOC estimation comparison using the LFP-1RC model during FUDS cycles with noisy measurements at an ambient temperature of 25 °C.

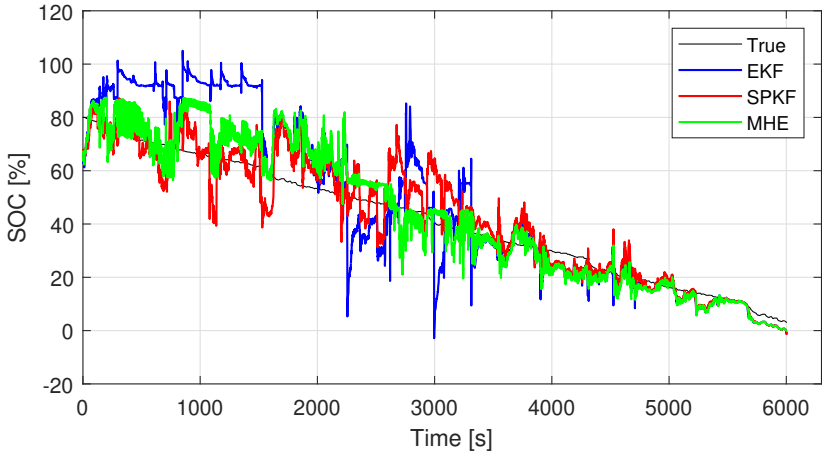

Figure 6.22: SOC estimation comparison using the LFP-ESC model during FUDS cycles with noisy measurements at an ambient temperature of 25 °C.

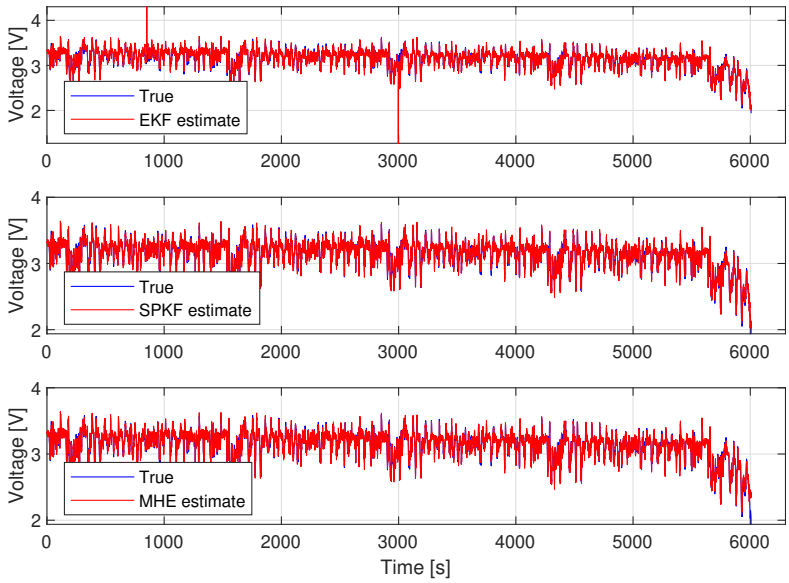

Figure 6.23: Output voltage estimation comparison using the LFP-ESC model during FUDS cycles with noisy measurements at an ambient temperature of 25 °C.

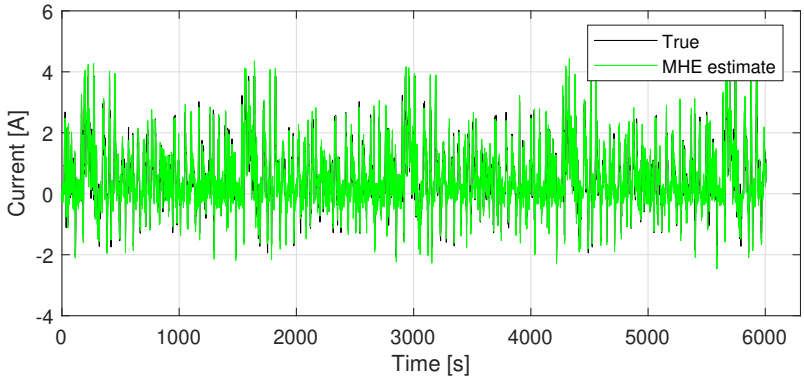

Figure 6.24: MHE load current estimation using the LFP-ESC model during FUDS cycles with noisy measurements at an ambient temperature of 25 °C.

	EKF		SPKF		MHE	
	RMSE	MAE	RMSE	MAE	RMSE	MAE
NMC-R	1.48 %	1.39 %	1.49 %	1.39 %	1.49 %	1.40 %
NMC-RC1	0.56 %	0.45 %	0.56 %	0.45 %	0.56 %	0.45 %
NMC-ESC	2.23 %	1.74 %	2.20 %	1.75 %	2.17 %	1.67 %
LFP-R	10.79 %	10.24 %	11.13 %	10.53 %	10.70 %	10.15 %
LFP-RC1	4.21 %	3.57 %	4.42 %	3.74 %	4.17 %	3.55 %
LFP-ESC	14.77 %	11.04 %	8.06 %	6.00 %	8.64 %	6.47 %

Table 6.10: Summary of SOC estimation RMSE and MAE for the estimators/model/cell combinations with noisy FUDS measurements.

	EKF		SPKF		MHE	
	RMSE	MAE	RMSE	MAE	RMSE	MAE
NMC-R	3.00 %	2.26 %	3.00 %	2.26 %	2.98 %	2.24 %
NMC-RC1	2.47 %	1.76 %	2.47 %	1.76 %	2.46 %	1.74 %
NMC-ESC	2.18 %	1.68 %	2.18 %	1.67 %	2.20 %	1.67 %
LFP-R	6.11 %	4.70 %	6.15 %	4.72 %	5.99 %	4.59 %
LFP-RC1	4.40 %	3.34 %	4.40 %	3.34 %	4.28 %	3.26 %
LFP-ESC	5.56 %	3.58 %	4.02 %	3.16 %	4.15 %	3.16 %

Table 6.11: Summary of output voltage estimation RMSE and MAE for the estimator/model/cell combinations with noisy FUDS measurements.

MHE load current estimate ($\hat{u}$)		
	RMSE	MAE
NMC-R	24.01 %	19.06 %
NMC-RC1	24.05 %	19.09 %
NMC-ESC	24.06 %	19.10 %
LFP-R	23.40 %	18.54 %
LFP-RC1	23.53 %	18.63 %
LFP-ESC	23.56 %	18.66 %

Table 6.12: Summary of the MHE load current estimation RMSE and MAE with noisy FUDS measurements.

6.4.3 Simulation 3 - Dynamic load with resting periods

In Figure 6.25 the comparison of the SOC estimates obtained from using the LFP-ESC model and FUDS with resting periods as input. This particular combination represents a best-performing LFP model in this simulation case. The corresponding voltage esti- mates can be observed in Figure 6.26. The load current estimates obtained from the MHE are shown in Figure 6.27. The same setup of plots is arranged for the best-performing NMC model, the NMC-1RC model, in Figure 6.28, Figure 6.29 and Figure 6.30. As previously, all results are summarized in Table 6.13, Table 6.14 and Table 6.15. For the discussion of the results, see Section 7.1.

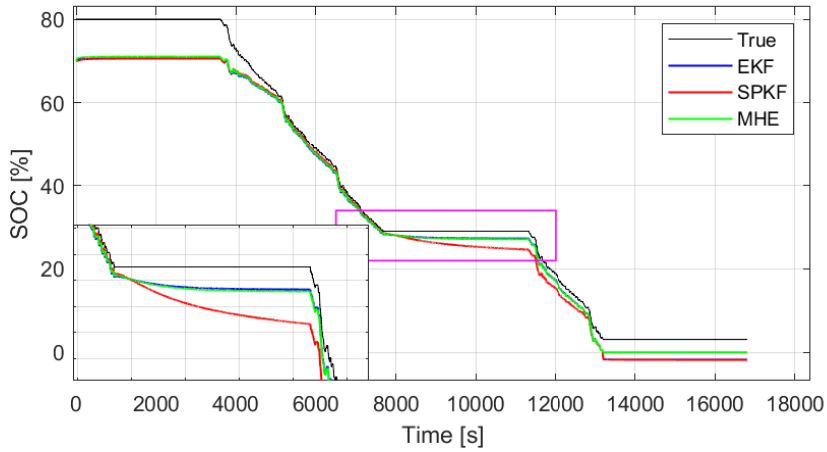

Figure 6.25: SOC estimation comparison using the LFP-ESC model during FUDS cycles with resting periods at an ambient temperature of 25 °C. An additional zoomed-in plot of the highlighted box period is added in the bottom left corner.

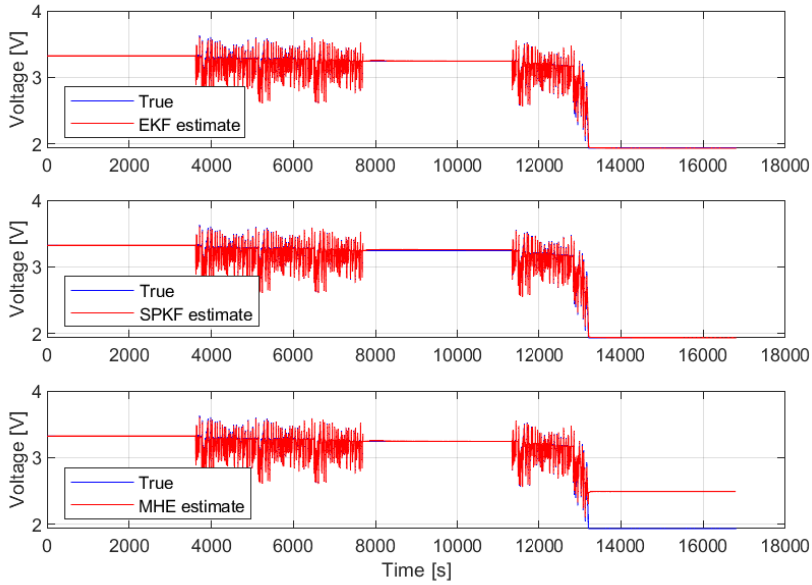

Figure 6.26: Output voltage estimation comparison using the LFP-ESC model during FUDS cycles with resting periods at an ambient temperature of 25 °C.

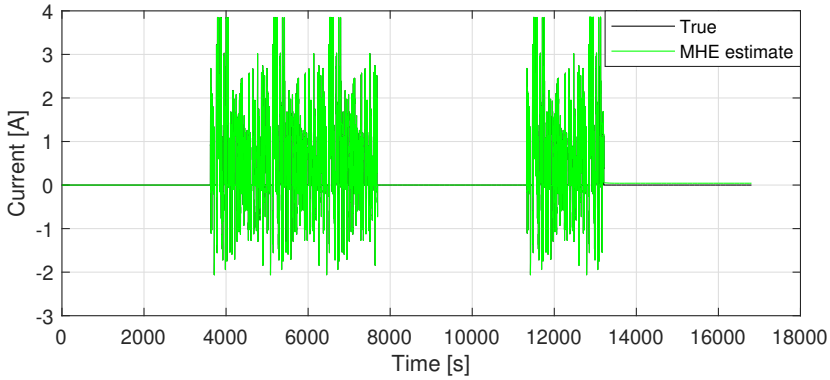

Figure 6.27: MHE load current estimation using the LFP-ESC model during FUDS cycles with resting periods at an ambient temperature of 25 °C.

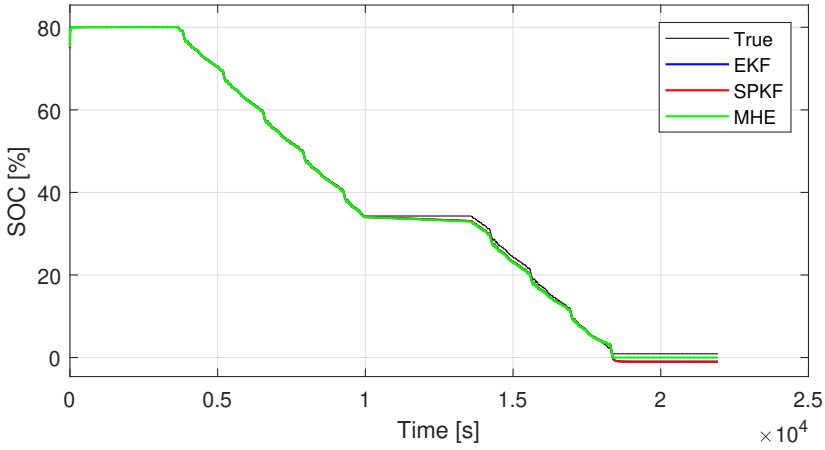

Figure 6.28: SOC estimation comparison using the NMC-1RC model during FUDS cycles with resting periods at an ambient temperature of 25 °C.

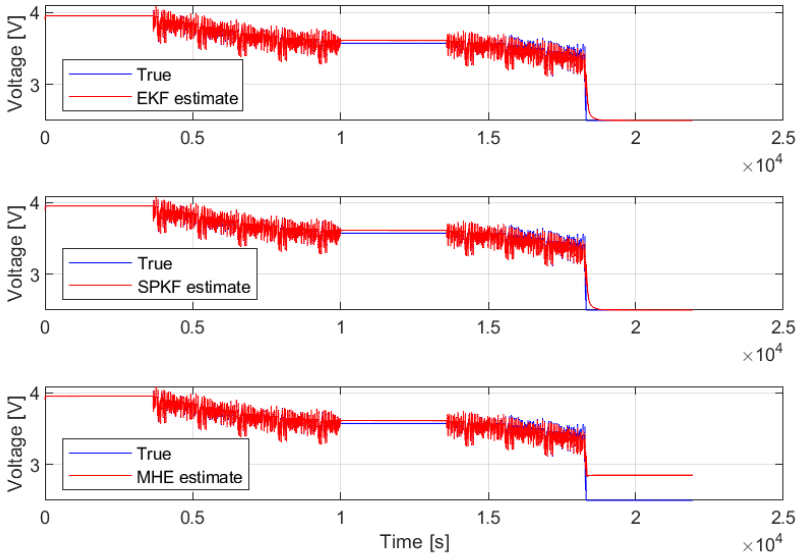

Figure 6.29: Output voltage estimation comparison using the NMC-1RC model during FUDS cycles with resting periods at an ambient temperature of 25 °C.

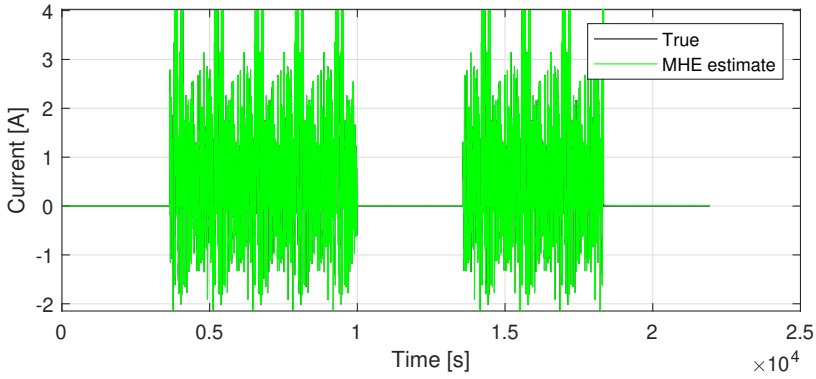

Figure 6.30: MHE load current estimation using the NMC-1RC model during FUDS cycles with resting periods at an ambient temperature of 25 °C.

	EKF		SPKF		MHE	
	RMSE	MAE	RMSE	MAE	RMSE	MAE
NMC-R	1.25 %	1.04 %	1.25 %	1.04 %	1.14 %	0.94 %
NMC-RC1	0.93 %	0.66 %	0.94 %	0.67 %	0.70 %	0.54 %
NMC-ESC	0.92 %	0.64 %	0.97 %	0.69 %	0.65 %	0.50 %
LFP-R	9.14 %	8.83 %	9.14 %	8.83 %	9.00 %	8.47 %
LFP-RC1	7.25 %	7.02 %	7.24 %	7.01 %	7.03 %	6.64 %
LFP-ESC	5.22 %	4.15 %	5.44 %	4.54 %	4.73 %	3.67 %

Table 6.13: Summary of SOC estimation RMSE and MAE for the estimators/model/cell combinations with resting periods added to the FUDS cycles.

	EKF		SPKF		MHE	
	RMSE	MAE	RMSE	MAE	RMSE	MAE
NMC-R	3.52 %	1.72 %	3.52 %	1.72 %	14.59 %	7.29 %
NMC-RC1	3.25 %	1.40 %	3.25 %	1.40 %	14.53 %	6.99 %
NMC-ESC	1.71 %	0.98 %	1.88 %	1.08 %	14.05 %	6.62 %
LFP-R	3.71 %	1.38 %	3.70 %	1.38 %	27.39 %	13.71 %
LFP-RC1	3.18 %	1.27 %	3.18 %	1.27 %	27.26 %	13.55 %
LFP-ESC	0.98 %	0.48 %	1.17 %	0.75 %	25.71 %	12.33 %

Table 6.14: Summary of output voltage estimation RMSE and MAE for the estimator/model/cell combinations with resting periods added to the FUDS cycles.

MHE load current estimate ($\hat{u}$)		
	RMSE	MAE
NMC-R	0.66 %	0.38 %
NMC-RC1	0.51 %	0.28 %
NMC-ESC	0.43 %	0.24 %
LFP-R	2.92 %	1.53 %
LFP-RC1	2.33 %	1.27 %
LFP-ESC	1.97 %	0.98 %

Table 6.15: Summary of the MHE load current estimation RMSE and MAE with resting periods added to the FUDS cycles.

7

Discussion

7.1 Results of SOC estimation

7.1.1 Estimator comparison

Based on all estimation results obtained in Section 6.4, it is clear that the SOC estimation accuracy of the EKF, SPKF, and MHE was practically indistinguishable. This was the case for almost all the test scenarios and model-cell type combinations. One discrepancy was when all estimators performed poorly with noise-corrupted measurements using the LFP-ESC model, as seen in Figure 6.22. Here the EKF performed notably worse than the other two. This may be attributed to the fact the EKF is based on a first-order linearization, which may render the EKF-based LFP-ESC model weakly observable or unobservable whenever the OCV derivative is zero. Thus when under the influence of noise, SOC estimation becomes troublesome. This reasoning is based on the observation that the largest estimation deviations were where the derivative of the NMC OCV curve is closest to zero. For example, observe the high SOC peaks around 50 % SOC in Figure 6.22. This is an area where the LFP OCV derivative is around zero, as seen in Figure 6.4.

The estimators' similar estimation performance was also reflected in the initialization analysis presented in Section 6.3. The surface plots show that each estimator could deliver high estimation accuracy if a sufficiently high initial covariance is set with a sufficiently close initial SOC guess. If the estimators had a really low initial covariance, meaning the confidence in the initial guess was high, and a poor initial SOC guess was chosen, it is clear that high SOC RMSE occurred. This was likely due to the convergence becoming a lot slower when the initial covariance is set really low. From the plots, it is also observed that the MHE and SPKF had a slightly better performance than the EKF if a zero SOC initial guess is set. On the opposite, the EKF had better performance if a 100 % initial SOC is set. Notice how much larger the errors became if the initial covariance value was below

$\sim 10^{-5}$.

The estimated output of the estimators for all cell-model combinations was also very similar, and overall accurate. When assuming perfect measurements with or without resting periods, the output voltage estimation results were below 4 %, and as low as ~ 1 % when using the 1RC model or the ESC model. When applying noisy measurements as inputs, these errors increased somewhat, as expected. One exception from accurate output voltage estimates is found in Table 6.14 for the MHE. Here the estimation error was much higher than the rest. This was due to the system constraints included in the MHE, which imposed a lower SOC bound of zero, forcing the estimated output to settle at the corresponding OCV. This is verified in e.g. Figure 6.28, where the EKF and SPKF SOC estimates reached below zero, whereas the MHE SOC estimates halted at zero.

Due to the choice of using multiple shooting when implementing the MHE, it was able to provide load current estimates. In simulations 1 and 3, the MHE estimated the battery load current with a very low estimation error, especially for the NMC cell. Both the RMSE and MAE were below 0.5 % for all cell-model combinations, which can be verified from e.g. Table 6.5 and Table 6.15. In simulation 2 when the measurements were corrupted by heavy noise, the results were poor with estimation errors around 20 %. Hence, under heavy noise on measurements, the MHE did not provide trustworthy load current estimates.

In the first simulation case, the estimators' average computation time per iteration was logged to compare their relative running times. In Table 6.6 it is obvious that MHE was computationally expensive, being approximately 1000 times slower than the Kalman filters. The difference in computational cost for the EKF and SPKF was negligible. Thus it can be argued that there is no incentive to choose the MHE above the simpler Kalman filters for the SOC estimation problem, other than the fact that the MHE is able to handle system constraints during estimation. Bearing in mind the theoretical and practical complexity of the SPKF, it may be reasonable to state that EKF was the best-performing state estimator by a small margin. It should be noted that tuning could have changed the outcome somewhat. Also, the implementation of a UKF, which has more tuning parameters than the CDKF, could have shown better results.

7.1.2 Influence of cell chemistry

In general, SOC estimation for the LFP cell was much more troublesome than for the NMC cell. The RMS SOC estimation error did not go lower than 2.49 % for any of the LFP models with any of the inputs. One thing to notice here was that estimation accuracy increased once the estimators were in the lower SOC range, where the OCV-SOC curve was more nonlinear and not as flat. This observation agrees with the remarks made on the observability requirements for the given ECMs in Section 5.4. It can be seen in Figure 6.4 that the LFP OCV derivative curve over the SOC range $\sim$ 15 % - 0.95 % often is close to zero and even crosses zero on multiple occasions. This induces weakly observable modes

and likely also unobservable modes for the LFP models, which causes decreased SOC estimation performance. More intuitively this can be explained by the fact that a small change in OCV voltage for the LFP cell causes a large change in SOC. Thus if the OCV-SOC relationship is not very accurate, SOC estimation error is expected.

The estimation results for the NMC cell were overall very accurate. In all test scenarios, all three estimators managed to achieve a SOC estimation error below 3%, and as low as ~ 0.5 % when using the 1RC model. When compared to the LFP cell, this was reasonable due to the more nonlinear, distinctive, and steeper OCV-SOC curve, which likely enables a higher degree of observability for the NMC-based models. Intuitively, a monotonic and steeper OCV-SOC curve yields more room for error because a small error in OCV corresponds to a small error in SOC. Thus any error in OCV does not heavily propagate into the following SOC estimates.

7.1.3 Model comparison

When evaluated over all three simulation cases and both cell types, the 1RC model gave the best and most consistent SOC estimation results. Especially in simulation case 2 with heavy noise on the measurements, the 1RC model gave more accurate SOC estimates by some distance, highlighting its possibly superior robustness over the other models against noise. It can be argued that the use of the average OCV-SOC curves provided sufficient coverage for errors introduced by voltage hysteresis. The overall good performance of the 1RC model highlights the significance of modeling the diffusion dynamics in a LIB. This argument is based on the notable increase in SOC estimation accuracy when compared to using the R model, which neglects the slow diffusion dynamics. That being said, the ESC model also performed well with certain exceptions. These exceptions were more extreme for the LFP cell, where the ESC model performed inconsistently with large variations.

In simulation case 3 in Section 6.4.3, the steady-state estimation performance of the estimators was looked into. For the LFP cell, as seen in Figure 6.25, the estimated initial SOC of the model was around 70%. From the initial voltage measurement and the corresponding voltage on the average OCV-SOC curve, it could be verified that this in fact mapped to that particular SOC. Thus using the average SOC curve instead of the discharge or charge OCV curves lead to an initial SOC estimation error of around 10%. Here it should be noted that the previous sign of the load current in the ESC model was unknown, so the hysteresis elements in the model were not able to counter the hysteresis effect initially. In the middle resting period, the last sign of the current was known, and therefore the smaller deviation in SOC could be caused by the activated hysteresis elements in the model. At lower temperatures where nonlinear hysteresis is a more significant factor [30], it can be argued that the ESC model is beneficial to use, in particular for LFP cells. One thing to notice in the scenario in the zoomed-in window in Figure 6.25. Further, it was noted that in simulation 3, applying zero load current to the ESC model did not seem to cause any major observability issues, as suggested in Section 5.4.

The best-performing model for the LFP cell over all the simulations was actually the R model during US05 cycles in Section 6.4.1. This is however in contrast with the trend shown during FUDS cycles, where it performed the worst. In fact, all the SOC estimation results for the LFP cell were inconsistent based on the model choice for simulation 1. However, the performance during FUDS cycles is more in line with trends shown in the other two simulation cases, where the 1RC model showed the most consistency. This is sensible since these were also based on the FUDS cycles with added noise or resting periods. The reason for the difference in estimation results during US06 cycles for the LFP cell might be the difference in demanded power from the LIB. The FUDS cycles simulate urban city driving and the US06 simulates more consistently aggressive and more power-demanding highway driving, hence the difference in demanded power combined with a very flat OCV curve may have been the cause of this large discrepancy. For the NMC cell, all models followed the same trends during both cycles.

7.2 Limitations

The limitations of the work in this thesis are a few. Temperature is a factor that impacts the accuracy of SOC estimation, and all experimentation conducted in this thesis has been performed with the assumption of a constant ambient temperature (25 °C) for the LIB cells. The OCV-SOC curves change as temperature changes, and it is important that this is accounted for if any state estimator is to be readily implemented in a BMS [21]. As mentioned earlier, nonlinear hysteresis, for instance, is more significant at lower temperatures.

For model-based estimation, the importance of model identification should not be underestimated. Referring to the remark made on model identification in Section 5.3, it was observed that depending on what SOC range the model identification was performed over, different model parameters were obtained. The final parameter values were also equally dependent on their initial values before applying the nonlinear regression method. This was especially true for the ESC model, which contained 6 model parameters and was the only model with a nonlinear state equation. Thus it may be the case that some optimization of the model identification procedure used herein could have resulted in an increased estimation performance. One should be aware that this involves the risk of overfitting the models [21].

7.3 Further work

Due to the broad scope of this thesis, this section mentions some of the areas further work can focus on. These topics are mentioned in a recent study in [4] as challenges that are still relevant in Battery Management Systems in 2023.

Further work can include a LIB cell´s dependence on temperature in the modeling, and evaluate the estimators' performance across a range of different temperatures. These are more realistic circumstances for the battery. Moreover, the parameters in the models used

herein are in reality time-varying. This means that a BMS should be able to update the parameters in real time along the lifespan of the LIBs. This is called co-estimation since a state estimator estimates the internal states and important model parameters in parallel. This is a difficult task due to the nonlinear and noise-sensitive behavior in LIBs. In EV applications, temperature and noise variations can be significant.

Moreover, further work can with benefit include state estimation of the other important internal states in the battery. These are for example the cell or battery's state of health (SOH), state of power (SOP), and state of energy (SOE). Many of these states depend on the SOC of the battery, which has motivated the use of joint estimation techniques, which can be further developed [4].

On another note, further development of the estimators themselves may also be interesting. The NLP in the MHE may be formulated in many ways, as for instance in [13]. Hence different formulations of the mathematical program to be solved each iteration could be further investigated. This includes ways of approximating the arrival cost, where alternatives to extended Kalman filter covariance updates have been looked into [54].

8

Conclusion

This master thesis has presented a comparison of the EKF, SPKF and MHE for SOC estimation using nonlinear ECMs for two different LIB cell chemistries. The two cell chemistries were the NMC cell and the LFP cell which differed significantly in open-circuit voltage characteristics. The ECMs were namely the R, the 1RC, and the ESC model, listed in order of increasing complexity. The estimators demonstrated a comparable and very similar SOC estimation performance, with SOC RMS estimation errors reaching as low as 0.5 % for an NMC cell using a 1RC or ESC model, and 2.5 % for an LFP cell using an R model assuming perfect measurements. Overall the estimation error increased somewhat for the estimators under the impact of noisy measurements or inputs with long resting periods. The MHE required an average computation time per iteration 1000 times higher than that of the Kalman filters, highlighting the computational complexity introduced by solving an NLP for every iteration in the MHE. Based solely on these results, other than providing system constraint handling, there would be low motivation for using the MHE above the EKF or SPKF for SOC estimation. Thus, due to the difference in theoretical complexity for the EKF and SPKF and the very similar estimation results, it can be argued that the EKF was marginally the best-performing estimator. On another note, the SOC estimation for LFP cells was evidently more difficult than for NMC-type cells. This was likely due to the flat OCV-SOC curve imposing observability issues on the LFP-based ECMs. When comparing the influence of model choice, the 1RC model outperformed the simpler R model for SOC estimation accuracy overall. The performance relative to the ESC model was on occasion comparable, but sometimes also better, especially with noise-corrupted measurements. Thus it is reasonable to assume that the 1RC model was the better-performing model. One discrepancy was for the LFP cell during US06 cycles, where the R model outperformed the other two by some distance, indicating that the type of dynamic load profile is of significance for SOC estimation in LFP cells.

Bibliography

[1] Taehoon Kim, Wentao Song, Dae-Yong Son, Luis K. Ono, and Yabing Qi. Lithium-ion batteries: outlook on present, future, and hybridized technologies. *J. Mater. Chem. A*, 7:2942–2964, 2019.

[2] Muhammad Umair Mutarraf, Yajuan Guan, Luona Xu, Chun-Lien Su, Juan C. Vasquez, and Josep M. Guerrero. Electric cars, ships, and their charging infrastructure – a comprehensive review. *Sustainable Energy Technologies and Assessments*, 52:102177, 2022.

[3] Alberto Danese, Bendik Nybakk Torsæter, Andreas Sumper, and Michele Garau. Planning of high-power charging stations for electric vehicles: A review. *Applied Sciences*, 12(7), 2022.

[4] Long Zhou, Xin Lai, Bin Li, Yi Yao, Ming Yuan, Jiahui Weng, and Yuejiu Zheng. State estimation models of lithium-ion batteries for battery management system: Status, challenges, and future trends. *Batteries*, 9(2), 2023.

[5] Marcin Kolodziejski and Iwona Michalska-Pozoga. Battery energy storage systems in shipsrsquo; hybrid/electric propulsion systems. *Energies*, 16(3), 2023.

[6] Jichao Hong, Zhenpo Wang, Fei Ma, Jue Yang, Xiaoming Xu, Changhui Qu, Jinghan Zhang, Tongxin Shan, Yankai Hou, and Yangjie Zhou. Thermal runaway prognosis of battery systems using the modified multiscale entropy in real-world electric vehicles. *IEEE Transactions on Transportation Electrification*, 7(4):2269–2278, 2021.

[7] Fengchun Sun, Rui Xiong, and Hongwen He. Estimation of state-of-charge and state-of-power capability of lithium-ion battery considering varying health conditions. *Journal of Power Sources*, 259:166–176, 2014.

[8] Yujie Wang, Jiaqiang Tian, Zhendong Sun, Li Wang, Ruilong Xu, Mince Li, and Zonghai Chen. A comprehensive review of battery modeling and state estimation approaches for advanced battery management systems. *Renewable and Sustainable Energy Reviews*, 131:110015, 2020.

[9] Neha Bhushan, Saad Mekhilef, Kok Soon Tey, Mohamed Shaaban, Mehdi Seyedmahmoudian, and Alex Stojcevski. Overview of model- and non-model-based online battery management systems for electric vehicle applications: A comprehensive review of experimental and simulation studies. *Sustainability*, 14(23), 2022.

[10] Prashant Shrivastava, Tey Kok Soon, Mohd Yamani Idna Bin Idris, and Saad Mekhilef. Overview of model-based online state-of-charge estimation using kalman filter family for lithium-ion batteries. *Renewable and Sustainable Energy Reviews*, 113:109233, 2019.

[11] Prashant Shrivastava, Tey Kok Soon, Mohd Yamani Idna Bin Idris, and Saad Mekhilef. Overview of model-based online state-of-charge estimation using kalman filter family for lithium-ion batteries. *Renewable and Sustainable Energy Reviews*, 113:109233, 2019.

[12] Ma Yan, Zhou Xiuwen, and Zhang Jixing. Lithium-ion battery state of charge estimation based on moving horizon. pages 5002–5007, 2014.

[13] Zhongbao Wei, Jian Hu, Yang Li, Hongwen He, Weihan Li, and Dirk Uwe Sauer. Hierarchical soft measurement of load current and state of charge for future smart lithium-ion batteries. *Applied Energy*, 307:118246, 2022.

[14] Jia-Ni Shen, Yi-Jun He, Zi-Feng Ma, Hong-Bin Luo, and Zi-Feng Zhang. Online state of charge estimation of lithium-ion batteries: A moving horizon estimation approach. *Chemical Engineering Science*, 154:42–53, 2016. Recent Advances in Energy Conversion and Storage Devices.

[15] A robust approach to state of charge assessment based on moving horizon optimal estimation considering battery system uncertainty and aging condition. *Journal of Cleaner Production*, 270:122508, 2020.

[16] Manh-Kien Tran, Andre DaCosta, Anosh Mevawalla, Satyam Panchal, and Michael Fowler. Comparative study of equivalent circuit models performance in four common lithium-ion batteries: Lfp, nmc, lmo, nca. *Batteries*, 7(3), 2021.

[17] Daniel D. Svendsen. *A Comparison of ECM-based State-of-Charge Estimators for Lithium-Ion Batteries*. NTNU, 2022.

[18] Yuqing Chen, Yuqiong Kang, Yun Zhao, Li Wang, Jilei Liu, Yanxi Li, Zheng Liang, Xiangming He, Xing Li, Naser Tavajohi, and Baohua Li. A review of lithium-ion battery safety concerns: The issues, strategies, and testing standards. *Journal of Energy Chemistry*, 59:83–99, 2021.

[19] Reiner Korthauer. *Lithium-Ion Batteries: Basics and Applications*. 2018.

[20] Robert C. Massé, Chaofeng Liu, Yanwei Li, Liqiang Mai, and Guozhong Cao. Energy storage through intercalation reactions: electrodes for rechargeable batteries. *National Science Review*, 4(1):26–53, 12 2016.

[21] G. L. Plett. *Battery Management Systems: Volume 1 - Battery Modeling*. Artech House, Massachusetts, United States of America, 2015.

[22] Ghassan Zubi, Rodolfo Dufo-López, Monica Carvalho, and Guzay Pasaoglu. The lithium-ion battery: State of the art and future perspectives. *Renewable and Sustainable Energy Reviews*, 89:292–308, 2018.

[23] Hubert Rubenbauer and Stefan Henninger. Definitions and reference values for battery systems in electrical power grids. *Journal of Energy Storage*, 12:87–107, 2017.

[24] Bizhong Xia, Bo Ye, and Jianwen Cao. Polarization voltage characterization of lithium-ion batteries based on a lumped diffusion model and joint parameter estimation algorithm. *Energies*, 15(3), 2022.

[25] Grzegorz Piłatowicz, Andrea Marongiu, Julia Drillkens, Philipp Sinhuber, and Dirk Uwe Sauer. A critical overview of definitions and determination techniques of the internal resistance using lithium-ion, lead-acid, nickel metal-hydride batteries and electrochemical double-layer capacitors as examples. *Journal of Power Sources*, 296:365–376, 2015.

[26] Jiaqiang Tian, Yujie Wang, and Zonghai Chen. An improved single particle model for lithium-ion batteries based on main stress factor compensation. *Journal of Cleaner Production*, 278:123456, 2021.

[27] Abbas Fotouhi, Daniel J. Auger, Karsten Propp, Stefano Longo, and Mark Wild. A review on electric vehicle battery modelling: From lithium-ion toward lithium–sulphur. *Renewable and Sustainable Energy Reviews*, 56:1008–1021, 2016.

[28] Anup Barai, W. Dhammika Widanage, James Marco, Andrew McGordon, and Paul Jennings. A study of the open circuit voltage characterization technique and hysteresis assessment of lithium-ion cells. *Journal of Power Sources*, 295:99–107, 2015.

[29] Federico Baronti, Nicola Femia, Roberto Saletti, Ciro Visone, and Walter Zamboni. Hysteresis modeling in li-ion batteries. *IEEE Transactions on Magnetics*, 50(11):1–4, 2014.

[30] G. L. Plett. *Battery Management Systems: Volume 2 - Equivalent-Circuit Methods*. Artech House, Massachusetts, United States of America, 2016.

[31] Gregory L. Plett. Sigma-point kalman filtering for battery management systems of lipb-based hev battery packs: Part 1: Introduction and state estimation. *Journal of Power Sources*, 161(2):1356–1368, 2006.

[32] M.S. Bazaraa, H.D. Sherali, and C.M. Shetty. *Nonlinear Programming Theory and Algorithms*. John Wiley Sons, Inc., New York, 2006.

[33] J. Nocedal and S. J. Wright. *Numerical Optimization*. Springer, second edition, 2006.

[34] Mohamed Mehrez. Optimization based solutions for control and state estimation in dynamical systems (implementation to mobile robots) a workshop, 01 2019.

[35] Moritz Diehl. Numerical optimal control. 07 2011.

[36] Moritz Diehl, Hans Joachim Ferreau, and Niels Haverbeke. *Efficient Numerical Methods for Nonlinear MPC and Moving Horizon Estimation*. Springer Berlin Heidelberg, Berlin, Heidelberg, 2009.

[37] Shi Zhao, Stephen R. Duncan, and David A. Howey. Observability analysis and state estimation of lithium-ion batteries in the presence of sensor biases. *IEEE Transactions on Control Systems Technology*, 25(1):326–333, 2017.

[38] Hongwen He, Rui Xiong, and Jinxin Fan. Evaluation of lithium-ion battery equivalent circuit models for state of charge estimation by an experimental approach. *Energies*, 4(4):582–598, 2011.

[39] Gregory L. Plett. Extended kalman filtering for battery management systems of lipb-based hev battery packs: Part 1. background. *Journal of Power Sources*, 134(2):252–261, 2004.

[40] Andreas Manthopoulos and Xiang Wang. A review and comparison of lithium-ion battery soc estimation methods for electric vehicles. In *IECON 2020 The 46th Annual Conference of the IEEE Industrial Electronics Society*, pages 2385–2392, 2020.

[41] Jiahao Li, Joaquin Klee Barillas, Clemens Guenther, and Michael A. Danzer. A comparative study of state of charge estimation algorithms for lifepo4 batteries used in electric vehicles. *Journal of Power Sources*, 230:244–250, 2013.

[42] E.A. Wan and R. Van Der Merwe. The unscented kalman filter for nonlinear estimation. In *Proceedings of the IEEE 2000 Adaptive Systems for Signal Processing, Communications, and Control Symposium (Cat. No.00EX373)*, pages 153–158, 2000.

[43] *An Evaluation of the Moving Horizon Estimation Algorithm for Online Estimation of Battery State of Charge and State of Health*, volume Volume 4B: Dynamics, Vibration, and Control of *ASME International Mechanical Engineering Congress and Exposition*, 11 2014. V04BT04A049.

[44] Christopher V. Rao and James B. Rawlings. Constrained process monitoring: Moving-horizon approach. *AIChE Journal*, 48(1):97–109, 2002.

[45] Fangdan Zheng, Yinjiao Xing, Jiuchun Jiang, Bingxiang Sun, Jonghoon Kim, and Michael Pecht. Influence of different open circuit voltage tests on state of charge online estimation for lithium-ion batteries. *Applied Energy*, 183:513–525, 2016.

[46] Yinjiao Xing, Wei He, Michael Pecht, and Kwok Leung Tsui. State of charge estimation of lithium-ion batteries using the open-circuit voltage at various ambient temperatures. *Applied Energy*, 113:106–115, 2014.

[47] Lithium Werks. *Specs for APR18650M1B*, 2019.

[48] Wei He, Nicholas Williard, Chaochao Chen, and Michael Pecht. State of charge estimation for li-ion batteries using neural network modeling and unscented kalman filter-based error cancellation. *International Journal of Electrical Power Energy Systems*, 62:783–791, 2014.

[49] Hamidreza Movahedi, Ning Tian, and Rajesh Rajamani. Hysteresis compensation and nonlinear observer design for state-of-charge estimation using a nonlinear double-capacitor li-ion battery model. *IEEE/ASME Transactions on Mechatronics*, PP:1–1, 03 2021.

[50] Yebin Wang, Huazhen Fang, Lei Zhou, and Toshihiro Wada. Revisiting the state-of-charge estimation for lithium-ion batteries: A methodical investigation of the extended kalman filter approach. *IEEE Control Systems Magazine*, 37(4):73–96, 2017.

[51] Anirudh Allam and Simona Onori. Linearized versus nonlinear observability analysis for lithium-ion battery dynamics: Why respecting the nonlinearities is key for proper observer design. *IEEE Access*, 9:163431–163440, 2021.

[52] M.W. Mehrez. Mpc and mhe implementation in matlab using casadi. `https://github.com/MMehrez/MPC-and-MHE-implementation-in-MATLAB-using-Casadi`, 2021.

[53] M.W. Mehrez. Mpc and mhe implementation in matlab using casadi — part 2. `https://www.youtube.com/watch?v=UCyZUCp1Bvs&list=PLK8squHT_Uzej3UCUHjtOtm5X7pMFSgAL&index=3&t=3017s&ab_channel=MohamedW.Mehrez`, 2019.

[54] Rodrigo López-Negrete, Sachin C. Patwardhan, and Lorenz T. Biegler. Constrained particle filter approach to approximate the arrival cost in moving horizon estimation. *Journal of Process Control*, 21(6):909–919, 2011.

[55] HongWen He, YongZhi Zhang, Rui Xiong, and Chun Wang. A novel gaussian model based battery state estimation approach: State-of-energy. *Applied Energy*, 151:41–48, 2015.

[56] Yuejiu Zheng, Minggao Ouyang, Xuebing Han, Languang Lu, and Jianqiu Li. Investigating the error sources of the online state of charge estimation methods for lithium-ion batteries in electric vehicles. *Journal of Power Sources*, 377:161–188, 2018.

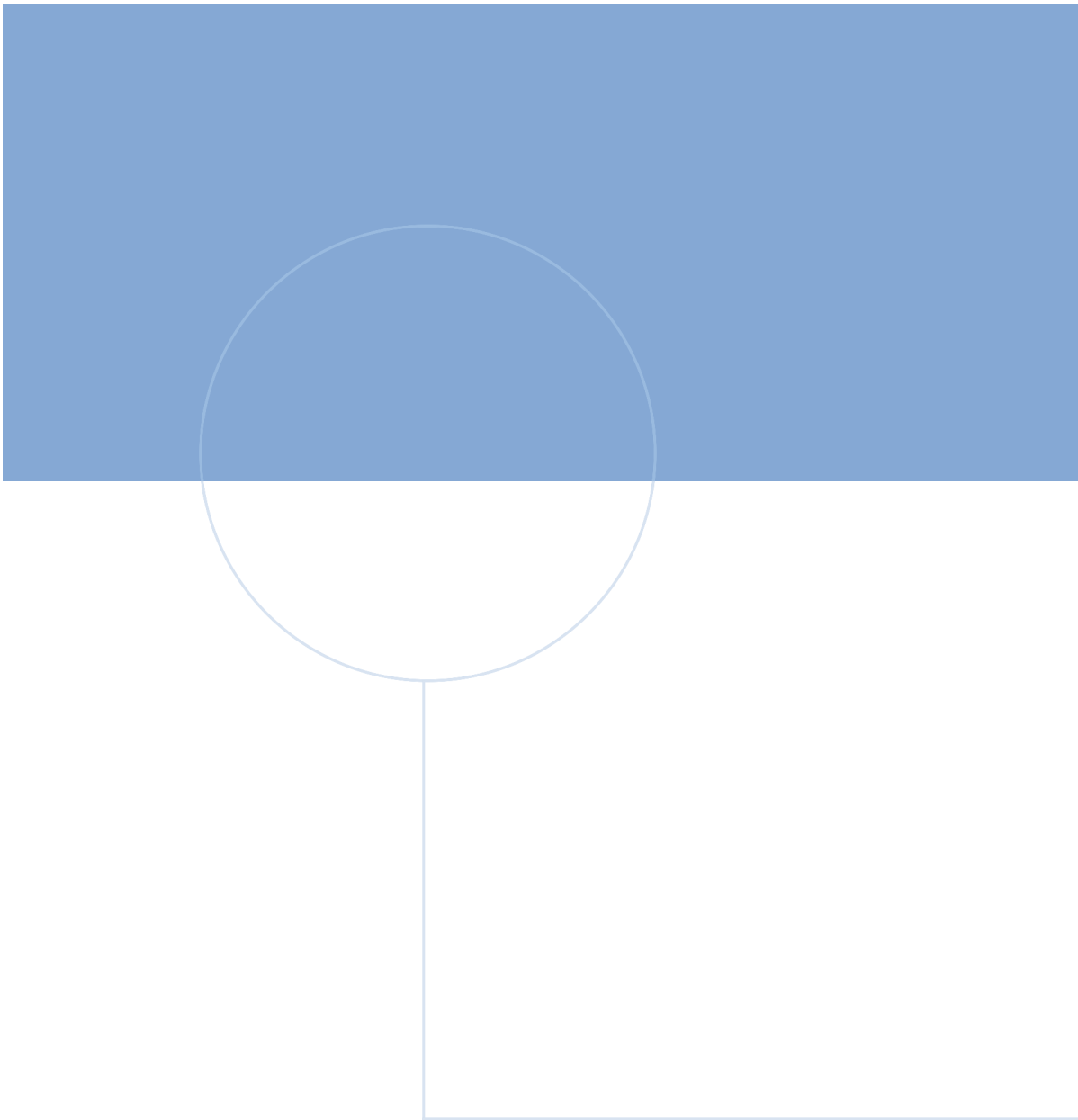

NTNU

Norwegian University of
Science and Technology